

Design of a multifunctional polar metal via first-principles high-throughput structure screening

Yue-Wen Fang^{1,2*} and Hanghui Chen^{2,3†}

¹*Department of Materials Science and Engineering,*

Kyoto University, Kyoto, Japan

²*NYU-ECNU Institute of Physics,*

New York University Shanghai, Shanghai, China

³*Department of Physics,*

New York University, New York, USA

(Dated: February 6, 2020)

Abstract

Intrinsic polar metals are rare, especially in oxides, because free electrons screen electric fields in a metal and eliminate the internal dipoles that are needed to break inversion symmetry. Here we use first-principles high-throughput structure screening to predict a new polar metal in bulk and thin film forms. After screening more than 1000 different crystal structures, we find that ordered BiPbTi₂O₆ can crystallize in three polar and metallic structures, which can be transformed between each other via pressure or strain. In a heterostructure of layered BiPbTi₂O₆ and PbTiO₃, multiple states with different relative orientations of BiPbTi₂O₆ polar displacements, and PbTiO₃ polarization, can be stabilized. At room temperature the interfacial coupling enables electric fields to first switch PbTiO₃ polarization and subsequently drive 180° change of BiPbTi₂O₆ polar displacements. At low temperature, the heterostructure provides a tunable tunnelling barrier and might be used in multi-state memory devices.

* fyuwen@gmail.com

† hanghui.chen@nyu.edu

Polar metals—analogy of ferroelectrics in metals—are characterized by intrinsic conduction and inversion symmetry breaking. Polar metals are rare (especially in oxides) because mobile electrons screen electric fields in a metal and eliminate internal dipoles that are needed to break inversion symmetry. The discovery of LiOsO_3 [1], a metal that transforms from a centrosymmetric $R\bar{3}c$ structure to a polar $R3c$ structure at 140 K, has stimulated an active search for new polar metals in both theory and experiment [2–9].

Density-functional-theory-based first-principles calculations have proven accurate in describing crystal structures and have been successfully applied to predict new functional materials, such as ferroelectrics, piezoelectrics and multiferroics [10]. Since crystal structure is the essential property of polar metals, we need to scrutinize the prediction by not presupposing an *a priori* favorable crystal structure. First-principles high-throughput crystal structure screening method, which is based on the marriage between first-principles calculations and a multitude of techniques such as particle-swarm optimization algorithm [11] and evolutionary algorithm [12], has demonstrated its superior power in effectively searching for the ground state structures and metastable structures of functional materials with only the given knowledge of chemical composition [13–15].

In this work, we use *ab initio* high-throughput structure screening to predict a new polar metal $\text{BiPbTi}_2\text{O}_6$ (BPTO for short). After screening over 1000 different crystal structures, we find that ordered BPTO can crystallize in three different polar metallic structures (post-perovskite $Pmm2$, perovskite $Pmm2$ and perovskite $Pmn2_1$), each of which can be transformed to another via external pressure or epitaxial strain. The mechanism is that 6s lone-pair electrons of Bi and Pb ions tend to favor off-center displacements [10]. On the other hand, in the perovskite structures, Bi^{3+} and Pb^{2+} enforce a fractional valence on Ti, which leads to conduction; in the post-perovskite structure, strong hybridization between Bi/Pb 6p and O 2p states induces a finite density of states at the Fermi level.

Next we demonstrate potential applications of the new polar metal BPTO by studying a BPTO/ PbTiO_3 heterostructure. We find that different states in which BPTO polar displacements are parallel, anti-parallel and perpendicular to PbTiO_3 polarization can be stabilized in the heterostructure. 180° switching of BPTO polar displacements needs to surmount an energy barrier of about 58 meV per slab. This implies that at room temperature where thermal fluctuations can overcome the switching barrier, the interfacial coupling between the polarization and polar displacements enables an electric field to first switch

PbTiO₃ polarization and subsequently drive BPTO to change its polar displacements by 180°; at low temperatures where the switching barrier dominates over thermal fluctuations, the BPTO polar displacements can not be switched but the direction of PbTiO₃ polarization can be controlled by an electric field. This can stabilize three distinct states with different tunnelling barriers.

Results and discussion

Most stable crystal structures of bulk BPTO

The key question in predicting a new polar metal is to determine its crystal structure. Since ordered BPTO has not been synthesized in experiment, we perform a first-principles high-throughput search for the ground state structure using CALYPSO [11, 16] method, in combination with CrySPY [17]. In the search, we do not constrain ourselves in any *a priori* favorable crystal structure. We screen more than 1000 different crystal structures among which we consider different Bi/Pb ordering in perovskite structure: layered ordering, columnar ordering and rock-salt ordering; and we also consider many non-perovskite structures, including post-perovskite structure and hexagonal structure. The computational details of our first-principles calculations and high-throughput structure screening method are provided in **Methods**.

Fig. 1 shows ten lowest-energy crystal structures of BPTO from our calculations. The details of these ten crystal structures are available in Supplementary Table 1. The lowest energy structure is post-perovskite with a polar symmetry $Pmm2$ (space group No. 25). The crystal structure is explicitly shown in Fig. 1**b**. The TiO₆ octahedra are both corner-sharing and edge-sharing. The lack of inversion symmetry can be appreciated from Ti atoms which have strong polar displacements with respect to neighboring O atoms towards x -axis. The next two lowest-energy crystal structures are both perovskite with $Pmn2_1$ symmetry (space group No. 31) and $Pmm2$ symmetry (space group No. 25). Both $Pmn2_1$ and $Pmm2$ symmetries are polar. The two perovskite structures have almost the same energy. Fig. 1**c** shows the perovskite $Pmn2_1$ crystal structure. Bi and Pb atoms form a rock-salt ordering and their displacements with respect to O atoms in the xy plane make the crystal structure acentric. Fig. 1**d** shows the perovskite $Pmm2$ crystal structure. Bi and

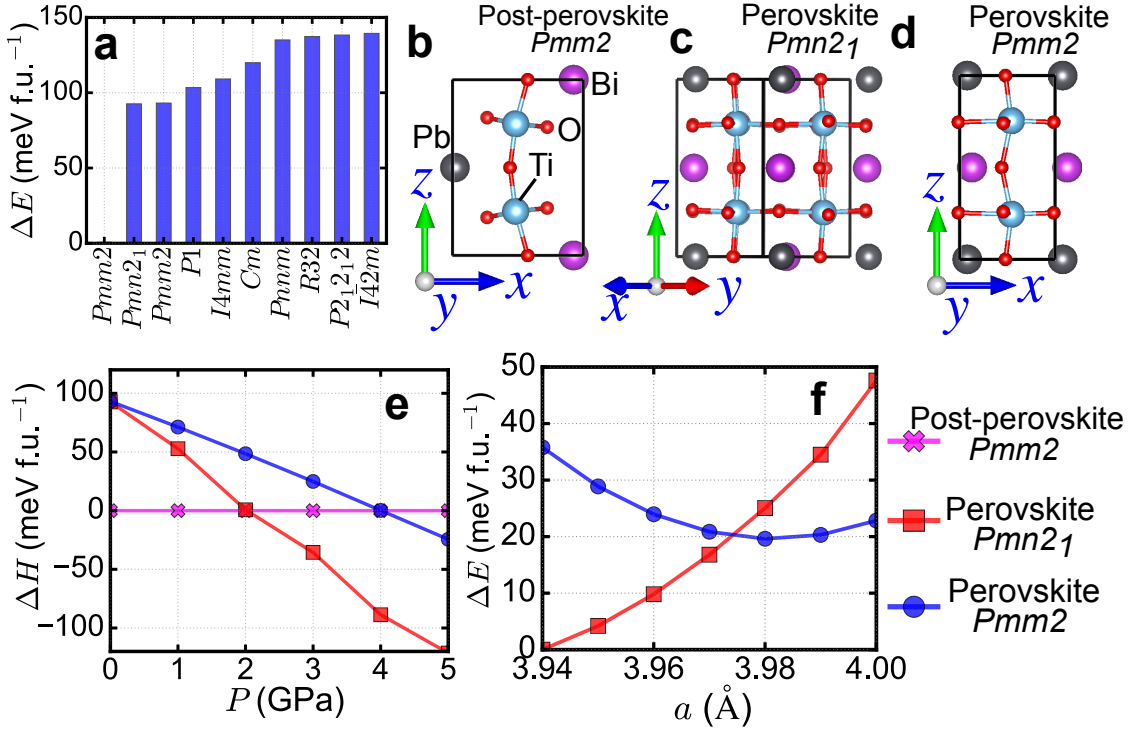


Fig. 1 The lowest-energy crystal structures and phase transitions. **a** Ten lowest-energy crystal structures of BPTO predicted by CALYPSO and DFT calculations. **b** Post-perovskite *Pmm2* structure; **c** Perovskite *Pmn21* structure; **d** Perovskite *Pmm2* structure. **e** Enthalpy of the three lowest-energy structures as a function of pressure. The enthalpy of the post-perovskite *Pmm2* structure under each pressure is set as the zero point. **f** Total energy of the two lowest-energy perovskite structures as a function of epitaxial strain. The energy of the perovskite *Pmn21* structure constrained by an in-plane lattice constant of 3.94 Å is chosen as the zero energy.

Pb atoms have a layered ordering with a stacking direction along *z*-axis. It is clear that Bi, Pb and Ti atoms all have strong polar displacements with respect to O atoms along *x*-axis, which breaks inversion symmetry. While post-perovskite oxides are interesting by themselves [18, 19], perovskite oxides have been widely studied and are more suitable for device applications because many perovskite oxide substrates are available [20], which makes it feasible to grow perovskite oxide thin films. Therefore, we consider using external pressure or epitaxial strain to transform BPTO among different polar structures. Pressure is widely used in bulk synthesis to isolate metastable phases of matter [21, 22]. Fig. 1e shows that both perovskite *Pmn21* and *Pmm2* structures become more stable than the post-perovskite

Pmm2 structure under a few GPa. The reason is that the post-perovskite *Pmm2* structure is very hollow with a very large volume of $130 \text{ \AA}^3 \text{ f.u.}^{-1}$ under ambient conditions, while the two perovskite structures are more closely packed ($122 \text{ \AA}^3 \text{ f.u.}^{-1}$ and $126 \text{ \AA}^3 \text{ f.u.}^{-1}$ under ambient conditions, respectively). Applying pressure favors structures with smaller volumes. If we want to grow BPTO thin films on a perovskite oxide substrate, the post-perovskite structure does not form due to very large lattice mismatch (see Supplementary Table 1 for the cell parameters of post-perovskite structure). The pseudo-cubic lattice constant of the perovskite *Pmn2₁* structure is 3.94 \AA , while that of the perovskite *Pmm2* structure is 3.98 \AA . It is anticipated that as the substrate lattice constant varies from 3.94 \AA to 3.98 \AA , the energetically favored structure changes from the perovskite *Pmn2₁* structure to the perovskite *Pmm2* structure. This is indeed what Fig. 1f shows. Since the perovskite *Pmm2* structure has a layered ordering of Bi/Pb atoms, it is highly suitable for thin film growth methods such as pulsed layer deposition and molecular beam epitaxy [23]. Substrates such as NdScO_3 and KTaO_3 have a proper lattice constant to stabilize the perovskite *Pmm2* structure in BPTO thin films. The DFT calculated lattice constants of KTaO_3 and NdScO_3 can be found in Supplementary Table 2 with the comparison to the experimental data. We also enforce the post-perovskite *Pmm2* structure to be stabilized on a perovskite oxide substrate and we expectedly find that its total energy is about 10 eV f.u.^{-1} higher than the two perovskite structures because of the large lattice mismatch (Supplementary Figure 1). In addition to the study of phase transitions under strains and pressures, the temperature effect on phase transitions can be found in Supplementary Figure 2.

Electronic and magnetic properties of polar metal BPTO

The upper panels of Fig. 2 show the DFT-calculated densities of states of the post-perovskite *Pmm2*, perovskite *Pmn2₁* and perovskite *Pmm2* structures. We calculate both total density of states (DOS) and orbital-projected DOS (Ti-3*d*, Bi-6*s*, Pb-6*s* and O-2*p*). In three optimized structures, we do not find any magnetization or charge disproportionation. Therefore spin-up and spin-down are summed in the DOS. The DOS projected on the two Ti atoms are identical and hence are also summed. The three DOS share similarities but also have important differences. All three structures have a non-zero DOS at the Fermi level; both Bi-6*s* and Pb-6*s* are well below the Fermi level and are fully occupied. The difference is

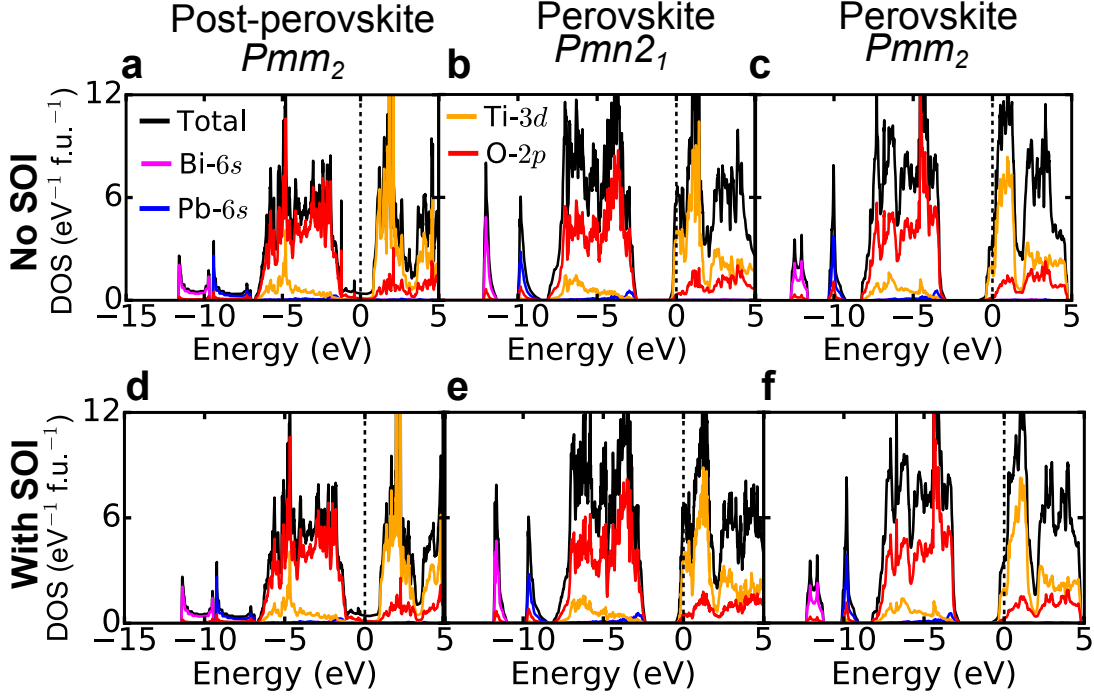


Fig. 2 Densities of states (DOS) of BPTO of the three polar structures. The upper and lower panels show the DOS calculated by DFT without spin-orbit interactions (SOI) and DFT with SOI, respectively. **a,d** The post-perovskite structure with Pmm_2 symmetry; **b,e** The perovskite structure with $Pmn2_1$ symmetry; **c,f** The perovskite structure with Pmm_2 symmetry. The black curve is the total DOS. The magenta, blue, orange and red curves are Bi-6s, Pb-6s, Ti-3d and O-2p projected DOS, respectively. The dashed line is the Fermi level.

that in both perovskite structures ($Pmn2_1$ and Pmm_2), because nominally Bi^{3+} , Pb^{2+} and O^{2-} , due to charge neutrality Ti must have a formal valence of $\text{Ti}^{3.5+}$, *i.e.*, every Ti atom has 0.5 electron in the 3d conduction bands (no charge disproportionation is found in the calculations). Figures. 2b and 2c show that the Fermi level crosses Ti-3d states in the DOS of the perovskite $Pmn2_1$ and Pmm_2 structures. However, in the post-perovskite structure (Fig. 2a), Ti-3d states have negligible contribution around the Fermi level. Instead, Bi-6p and Pb-6p as well as O-2p states make the largest contribution to the DOS around the Fermi level, which can also be seen in Supplementary Figure 3 where the electronic states around the Fermi level are zoomed in.

The Bader (static) charge analysis in Table 1 shows that Bi and Pb have about 0.25 and 0.19 more electrons in the post-perovskite structure than in the perovskite structures,

which indicates stronger hybridization between Bi/Pb and O atoms in the post-perovskite structure. Therefore in the post-perovskite structure, Bi-6*p* and Pb-6*p* states are not fully empty and thus appear around the Fermi level.

Table 1 Bader charges for bulk BPTO. Charges are normalized to per atom.

Structural type	Space group	Bader charges (<i>e</i>)			
		Bi	Pb	Ti	O
Post-perovskite	<i>Pmm2</i>	+1.48	+1.13	+2.19	-1.16
Perovskite	<i>Pmn2</i> ₁	+1.73	+1.35	+2.12	-1.22
Perovskite	<i>Pmm2</i>	+1.73	+1.32	+2.06	-1.19

Pb and Bi are heavy elements and their spin-orbit interactions (SOI) are not negligible. In the lower panels of Fig. 2, we take into account SOI and show the corresponding densities of states of BPTO of the three polar structures. Similar to the results without SOI, we do not find any magnetization or charge disproportionation in the fully relaxed structures. By comparing the densities of states calculated by DFT without SOI (upper panels of Fig. 2) and DFT with SOI (lower panels of Fig. 2), SOI almost unaffected the electronic structure, similar to previous studies on other polar metals [3, 24].

While DFT with/without SOI calculations do not find any magnetization or charge disproportionation, correlation effects from Ti-3*d* orbitals may favor spin ordering and charge ordering. A long-range magnetic ordering with a charge disproportionation (Ti³⁺+Ti⁴⁺) can result in an insulating ground state [25]. To test the robustness of our prediction that BiPbTi₂O₆ is a polar metal, we apply an effective Hubbard *U* correction on the Ti-3*d* orbitals and calculate the densities of states for all three low-energy structures. The accurate value of correlation strength of BPTO is not known, but presumably it should not exceed that of Mott insulator LaTiO₃, in which Hubbard *U*_{Ti} is about 5 eV [26]. Therefore we consider a Hubbard *U*_{Ti} ranging from 0 to 5 eV. Within this range of *U*_{Ti}, we do not find charge disproportionation but find robust metallicity in all the three polar structures of BPTO. Furthermore, in this range of *U*_{Ti}, we find itinerant ferromagnetism in the perovskite *Pmn2*₁ structure at *U*_{Ti} ≥ 1 eV and in the perovskite *Pmm2* structure at *U*_{Ti} ≥ 2 eV (antiferromagnetic ordering is less stable than ferromagnetic ordering). We do not find any magnetism in the post-perovskite *Pmm2* structure up to *U*_{Ti} = 5 eV. The magnetic phase diagram for

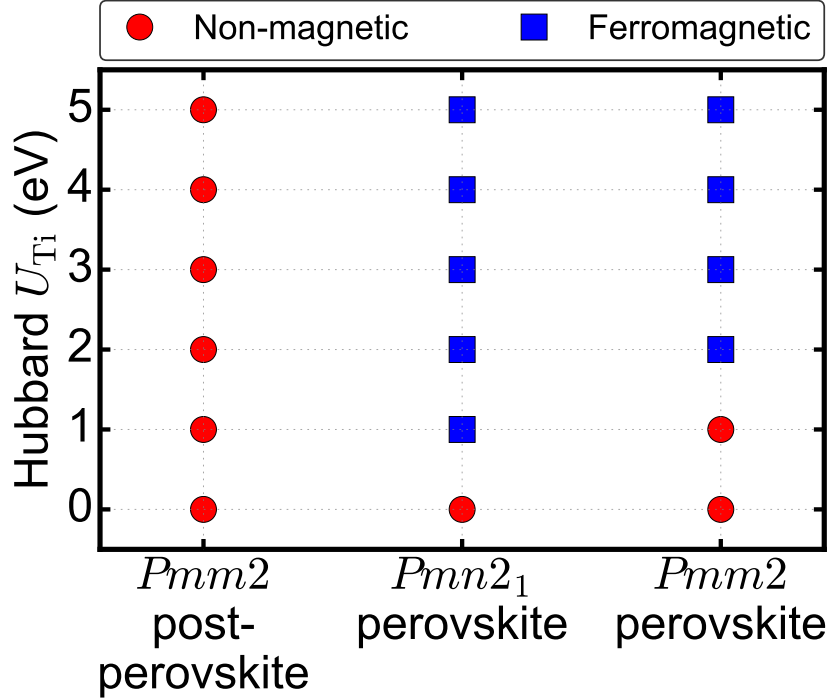


Fig. 3 Phase diagram as a function of Hubbard U . The magnetic phase diagram of the post-perovskite $Pmm2$, perovskite $Pmn2_1$ and perovskite $Pmm2$ structures as a function of Hubbard U_{Ti} . Non-magnetic state and ferromagnetic state are shown by red circle and blue square, respectively.

the three polar structures as a function of Hubbard U_{Ti} is shown in Fig. 3. The origin of itinerant ferromagnetism in BPTO is Stoner instability [27]. In DFT+ U calculations, the Stoner criterion to induce itinerant ferromagnetism is [28]:

$$U\rho(E_{\text{F}}) > 1, \quad (1)$$

were U and $\rho(E_{\text{F}})$ are Hubbard U parameter and density of states at the Fermi level of a non-magnetic state, respectively. The upper panels of Fig. 2 shows that the perovskite $Pmn2_1$ structure has a large density of state at the Fermi level $\rho(E_{\text{F}})$ in its non-magnetic state; the perovskite $Pmm2$ structure has a slightly smaller $\rho(E_{\text{F}})$. Post-perovskite $Pmm2$ structure, on the other hand, has a very small $\rho(E_{\text{F}})$ (9 times smaller than that of the perovskite $Pmm2$ structure and 15 times smaller than that of the perovskite $Pmn2_1$ structure). This explains that the critical U_{Ti} to stabilize itinerant ferromagnetism in the perovskite $Pmn2_1$ structure is the smallest, while a much larger U_{Ti} (larger than 5 eV) is needed to induce

magnetism in the post-perovskite $Pmm2$ structure.

The role of lone-pair electrons

A local structural instability arising from lone-pair electrons has been reported in ferroelectric insulators and degenerately doped ferroelectrics [10, 29–35]. However, lone-pair electrons alone are not sufficient to stabilize a polar state in metals nor a ferroelectric state in insulators. For example, BiFeO_3 is ferroelectric [30] but BiMnO_3 is anti-ferroelectric [36, 37] although lone-pair electrons are present in both of them. Therefore, high-throughput crystal structure prediction is essential in predicting new polar metals and ferroelectric insulators. In our study, the crystal structure screening takes into account both polar and anti-polar states for different cation orderings.

We now show that in the three lowest-energy metallic phases of BPTO, the lone-pair 6s electrons in Bi and Pb play an important role in breaking inversion symmetry. We use electron localization function (ELF, defined in **Methods**) to explicitly visualize how lone-pair electrons of Bi and Pb break inversion symmetry in metallic BPTO. The panels **a-c** of Fig. 4 show an iso-surface of ELF of the three polar structures of BPTO. Only the ELF of Bi and Pb ions are displayed for clarity. Similar to insulating Bi-based and Pb-based perovskite oxides [29, 30, 38], the ELF shows that a lobe-like lone-pair resides on one side of Bi and Pb ions in all three polar metallic structures, which is the driving force to break inversion symmetry. On the other hand, ELF in the corresponding centrosymmetric structures shows spherical-symmetric feature, which is implied in panels **d-f** of Fig. 4. Furthermore, we calculate the total energy variation as a function of normalized polar displacement λ from the centrosymmetric structures to the polar structures (see panels **g-i** of Fig. 4). In all three cases, the energy curve monotonically decreases from the centrosymmetric structure to the polar structure, which indicates a continuous and spontaneous phase transition below a critical temperature (satisfying Anderson’s and Blount’s criterion of a ferroelectric-like metal [39]). The energy difference between the polar structure and the corresponding centrosymmetric structure of BPTO in all three cases is larger than that of LiOsO_3 (about 25 meV f.u.⁻¹), implying that the structural transition temperature of BPTO is higher than that of LiOsO_3 [40]. We note that the above second-order structural phase transition is a key property to distinguish intrinsic polar metals from degenerately doped ferroelectrics

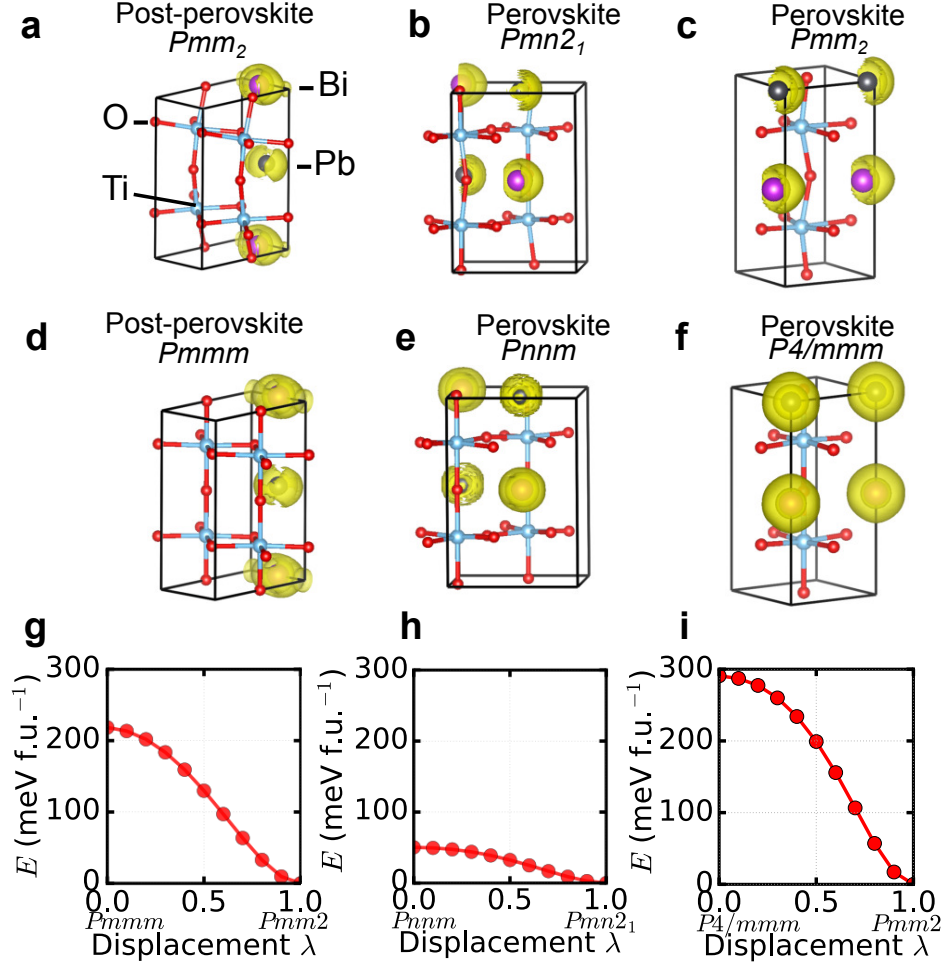


Fig. 4 Electron localization function (ELF) and the energy curve from the centrosymmetric structure to the corresponding polar structure. **a** The polar structure: post-perovskite Pmm_2 and **d** the centrosymmetric structure: post-perovskite $Pmmm$; **b** The polar structure: perovskite $Pmn2_1$ and **e** the centrosymmetric structure: perovskite $Pnmm$; **c** The polar structure: perovskite Pmm_2 and **f** the centrosymmetric structure: perovskite $P4/mmm$. The isosurface of ELF is set at a value of ~ 0.5 . **g** Transition from the post-perovskite $Pmmm$ structure to the post-perovskite Pmm_2 structure. **h** Transition from the perovskite $Pnmm$ structure to the perovskite $Pmn2_1$ structure. **i** Transition from the perovskite $P4/mmm$ structure to the perovskite Pmm_2 structure.

[32–35, 41, 42], because realistic dopants (cation substitution or oxygen vacancies) make the crystal symmetry of doped ferroelectrics ill-defined and correspondingly there is no well-defined continuous structural phase transition at finite temperatures.

Switching barrier of BPTO thin films in a heterostructure

Next we study BPTO thin films. The $Pmm2$ perovskite structure of BPTO, which has a layered Bi/Pb ordering, is highly suitable for thin film growth and can be stabilized on a perovskite oxide substrate having a lattice constant of 3.98 Å or larger. The Bi/Pb stacking direction in the $Pmm2$ perovskite structure is chosen as the z -axis, while the polar displacements are in the xy -plane. In addition, we find that constrained by an in-plane lattice constant of 3.98 Å or larger, ferroelectric PbTiO_3 is under tensile strain and favors an in-plane polarization over an out-of-plane polarization (Supplementary Figure 4). Therefore, we study a BPTO/ PbTiO_3 heterostructure, in which both BPTO polar displacements and PbTiO_3 polarization are parallel to the interface. We will show that different from previously studied ferroelectric/polar-metal heterostructures [2, 4, 43, 44], multiple states with different relative orientations of $\text{BiPbTi}_2\text{O}_6$ polar displacements and PbTiO_3 polarization can be stabilized. When an electric field is applied to switch the polarization of PbTiO_3 , a finite energy barrier exists for BPTO to change its polar displacements by 180°. If the temperature is high enough that thermal fluctuations can overcome the energy barrier, the polar displacements of BPTO will follow the change of PbTiO_3 polarization. Otherwise, the polar displacements of BPTO stay put and form different configurations when the external electric field changes the direction of PbTiO_3 polarization.

Fig. 5a shows a BPTO/ PbTiO_3 heterostructure. The in-plane lattice constant is constrained to 4 Å, which stabilizes both perovskite $Pmm2$ structure of BPTO and an in-plane polarization of PbTiO_3 . Experimentally substrates such as KTaO_3 and NdScO_3 can provide such a lattice constant. Fig. 5a shows two different configurations: on the left (right) is a “parallel state” (“anti-parallel state”) in which PbTiO_3 polarization is parallel (anti-parallel) to BPTO polar displacements. Both configurations are stabilized after relaxation in our calculations. We first find that one-unit-cell thin film of BPTO is still polar and metallic. Fig. 5b shows layer-resolved conduction electrons by integrating the partial density states of Ti- d orbitals (Supplementary Figure 5). Conduction electrons are mainly confined in BPTO with some charge leakage into a few unit cells of PbTiO_3 . This charge leakage is due to the proximate effect that Ti- d states in PbTiO_3 are empty while Ti- d states in BPTO nominally have 0.5 e per Ti atom. Such a charge leakage can be effectively prevented by replacing PbTiO_3 with $\text{PbTi}_{1-x}\text{Zr}_x\text{O}_3$ [45], which is supported by our calculations in Supplementary

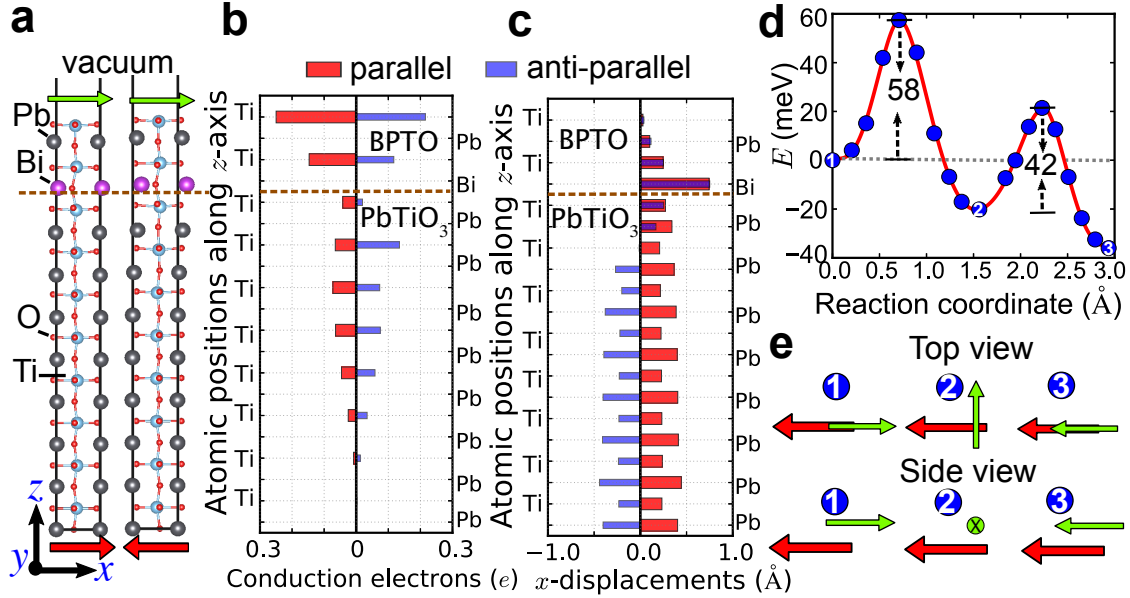


Fig. 5 Switching of polar displacements of BPTO in a BPTO/PbTiO₃ heterostructure. **a** Atomic structure of the BPTO/PbTiO₃ heterostructure: “parallel state” (left) and “anti-parallel state” (right). The red (green) arrow refers to PbTiO₃ polarization (BPTO polar displacement). **b** Layer-resolved conduction electrons on each Ti atom in parallel and anti-parallel states. **c** Layer-resolved polar displacements of metal ions along the x -axis in parallel and anti-parallel states. In **a**, **b** and **c**, the brown dashed lines indicate BPTO/PbTiO₃ interface. **d** Calculated energy barrier along the transition path from the anti-parallel state to the parallel state. The energy of anti-parallel state is set as the zero point. The black dashed arrows highlight two energy barriers. The blue circles represent the images on the transition path found in the nudged elastic band calculations. The three energy minima along the transition path are schematically shown in **e**: “1” is the anti-parallel state, “3” is the parallel state and “2” is a metastable state with BPTO polar displacements perpendicular to PbTiO₃ polarization in the xy plane.

Figure 6. Fig. 5c shows the layer-resolved cation displacements of Ti and Pb/Bi with respect to O atoms along the x -axis. The polar displacements of Bi and Pb in BPTO are almost bulk-like in both configurations. We note that the polar property of BPTO is not due to the interfacial coupling with PbTiO₃ (Supplementary Figure 7). With PbTiO₃ replaced by a paraelectric SrTiO₃ substrate, one-unit-cell BPTO layer still has polar displacements and is metallic (Supplementary Figure 8).

Next we study thermodynamics and the energy barrier of switching between “parallel state” and “anti-parallel state”. DFT calculations find that the energy of “parallel state” is 37 meV per slab lower than that of “anti-parallel state”. This is because in “anti-parallel state”, a 180° domain wall is formed in PbTiO_3 close to the interface, which is clearly seen from Fig. 5c. Forming such a 180° domain wall in ferroelectrics increases energy [46, 47]. Fig. 5c shows that in both configurations, the interface strongly favors a parallel coupling between BPTO polar displacements and PbTiO_3 polarization.

While “parallel state” is more stable than “anti-parallel state”, “anti-parallel state” can be stabilized by itself because it is a local minimum. Therefore a finite energy barrier exists for BPTO to 180° change its polar displacements from “anti-parallel state” to “parallel state”. To quantitatively calculate the energy barrier and identify a possible switching path for polar displacement, we perform the climbing image nudged elastic band (NEB) calculations [48] and use transition state theory [49]. Transition state theory has been widely used in understanding polarization switching in ferroelectric thin films [50, 51], as well as ferroelectric domain wall motion [52]. We choose “anti-parallel state” as the initial state and “parallel state” as the final state. We study a possible switching path in which BPTO polar displacements are 180° “rotated” in the xy plane. The NEB results are shown in Fig. 5d. Along the structural transition path from “anti-parallel state” (labelled as “1”) to “parallel state” (labelled as “3”), there is another metastable state (labelled as “2”) where BPTO polar displacements are perpendicular to PbTiO_3 polarization in the xy plane (Fig. 5e). Between the three stable states (“1”, “2”, “3”), there are two energy barriers. The larger one, *i.e.*, the energy difference between the anti-parallel state and the highest saddle point, is 58 meV per slab.

Multifunctions of the BPTO/PTO heterostructure

In this section, we discuss potential functions of the BPTO/PTO heterostructure based on the calculated switching barrier in the previous section.

We first discuss room temperature applications. The switching barrier of BPTO is about 58 meV per slab. From transition state theory [49], at a given temperature T , an energy barrier ΔE with a magnitude of a few $k_B T$ can be easily surmounted [53] (k_B is the Boltzmann constant). Room temperature $T = 300$ K is about 26 meV. Our energy barrier is

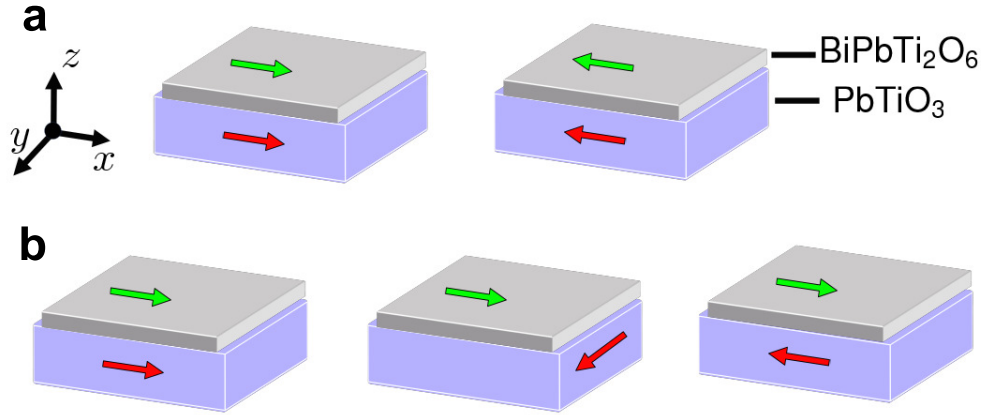


Fig. 6 Multifunctions of the BPTO/PbTiO₃ heterostructure. **a** At high temperature, the energy barrier is easily surmounted by thermal fluctuations and the polar displacements of BPTO can be switched. From the left panel to the right panel, as an electric field switches the polarization of PbTiO₃, the BPTO thin film follows the change and switches its polar displacements via the interfacial coupling. **b** At low temperature, the energy barrier can not be overcome and the polar displacements of BPTO get “stuck”. However, an electric field can switch the polarization of PbTiO₃ and stabilize multiple states with different orientation of PbTiO₃ polarization relative to the polar displacements of BPTO. Each state has different tunnelling barriers. From the left panel to the right panel, it is “parallel”, “perpendicular”, and “anti-parallel” state. The red arrow refers to the polarization of PbTiO₃ thin film. The green arrows refer to the polar displacements of BiPbTi₂O₆ thin film.

about twice room temperature and therefore room temperature is sufficient to overcome the barrier. This implies that the interfacial coupling at the BPTO/PbTiO₃ interface enables an electric field to first switch PbTiO₃ polarization and subsequently drive BPTO to 180° change its polar displacements. This realizes an electrically switchable bi-state in the new polar metal BPTO at room temperature. We note that the transition path chosen in the NEB calculation is only one possibility. The actual transition path could be different from the one in our study and the resulting energy barrier should be even lower, which will make the switching of BPTO polar displacements more feasible. Fig. 6a schematically shows how we can use PbTiO₃ polarization to control the polar displacements of BPTO at room temperature.

The above switching mechanism is also applicable to multi-layer BPTO thin films. The

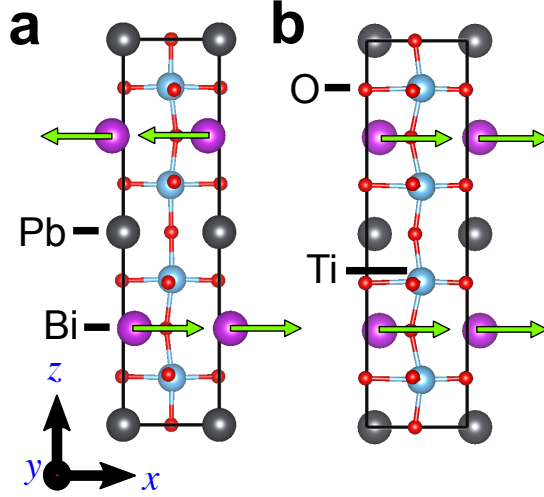


Fig. 7 The comparison between anti-polar and polar phases of BPTO. **a** The unit cell structure of anti-polar phase $Pmma$ of BPTO. **b** The two unit cells structure of polar phase $Pmm2$ of BPTO. The green arrows indicate the polar displacements of the Bi atoms.

mechanism is as follows. Our calculations find that bulk BPTO is more stable in the polar $Pmm2$ perovskite structure than the anti-polar $Pmma$ perovskite structure by 65 meV f.u.^{-1} . The anti-polar $Pmma$ perovskite structure is shown in Fig. 7a. The polar $Pmm2$ perovskite structure is shown in Fig. 7b for comparison. Therefore, for multi-layer BPTO thin films, once the bottom layer of BPTO is 180° switched via the interfacial coupling, the remaining layers of BPTO will be driven by thermodynamics to change their polar displacements in a layer-by-layer manner to avoid an anti-polar state in the film. The above physical picture is computationally confirmed in Supplementary Figure 9. However, for device applications, BPTO thin films of single-unit-cell thick are most desirable, in analogy to two-dimensional Van der Waals materials [9].

Next we discuss low temperature applications. At sufficiently low temperatures where the energy barrier is much larger than $k_B T$, the interfacial coupling can not drive polar metals to change their polar displacements when an electric field switches the polarization of ferroelectrics. However, this has interesting implications: as we use the electric field to change the direction of PbTiO_3 polarization, we can individually stabilize multiple configurations in which the BPTO polar displacements are “parallel”, “perpendicular” and “anti-parallel” to the PbTiO_3 polarization (shown in Fig. 6b). Each configuration has different tunnelling resistance across ferroelectric insulators, because BPTO polar displacements

and PbTiO_3 polarization have different relative orientation. As we use an electric field to change the direction of ferroelectric polarization (polar displacements do not follow due to low temperatures), we can tune tunnelling barriers between different states and therefore the BPTO/ PbTiO_3 heterostructure can be used in multi-state memory devices.

In conclusion, we demonstrate the power of first-principles high-throughput screening in designing new functional materials and in particular predict a new polar metal BPTO by utilizing the Bi/Pb lone-pair electrons. The three lowest-energy structures of BPTO are all polar and metallic (post-perovskite $Pmm2$, perovskite $Pmm2$ and perovskite $Pmn2_1$), which can be transformed among each other via pressure or strain. In the perovskite structures, Bi^{3+} and Pb^{2+} enforce a fractional valence 3.5+ on Ti, which leads to conduction. In the post-perovskite structure, strong hybridization between Pb/Bi $6p$ and O $2p$ states induces a finite density of states at the Fermi level. In a BPTO/ PbTiO_3 heterostructures, at room temperature the interfacial coupling can overcome the switching barrier, which enables an electric field to first switch PbTiO_3 polarization and subsequently drive BPTO to 180° flip its polar displacements. This realizes an electrically switchable bi-state in the new polar metal BPTO. The switching method is applicable to other layered polar metals [3]. At low temperature, an electric field can control the direction of PbTiO_3 polarization and stabilize multi states in which PbTiO_3 polarization and BPTO polar displacements have different relative orientations, implying different tunnelling resistance. This property can be used in tunable multi-state memory devices. We hope this work will stimulate experimentalists to synthesize the new polar metal in both bulk and thin-film forms.

Methods

First-principles calculations

For bulk structures, density functional theory (DFT) calculations are performed using a plane wave basis set and projector-augmented wave method [54], as implemented in the Vienna Ab-initio Simulation Package (VASP) [55, 56]. PBEsol, a revised Perdew-Burke-Ernzerhof (PBE) generalized gradient approximation for improving equilibrium properties of densely-packed solids [57], is used as the exchange correlation functional and has been applied successfully to interpreting the experimental observations of polar metal LiOsO_3

in our previous work [24]. The Brillouin zone integration is performed with a Gaussian smearing of 0.05 eV over a Γ -centered \mathbf{k} -mesh up to $12 \times 12 \times 12$ and a 600 eV plane-wave cutoff. The threshold of energy convergence is 10^{-6} eV. Hubbard U corrections are also considered in our calculations to model the effects of strong correlation on electronic and magnetic properties. The rotationally-invariant approach of Hubbard U proposed by Dudarev *et al.* [58] is used in our DFT+ U calculations. Spin-orbit coupling (SOC) is also considered to study electronic structure in our DFT+ U +SOC calculations [59].

For the calculations of BPTO/PbTiO₃ structures, a Γ -centered \mathbf{k} -mesh of $10 \times 10 \times 1$ is used. The periodic slabs are separated by vacuum of 20 Å thick to diminish the interaction between them. Since asymmetrical interface modelling is used in our calculations, we employ dipole correction to eliminate the artificial electric field in the vacuum [60, 61]. In all the interface calculations, the in-plane lattice constant is fixed to be 4 Å and the bottom layer of PbTiO₃ is fixed to simulate the bulk-like interior that is under tensile strain. All the other atoms are fully relaxed along the three axes. We consider two possible terminations of the heterostructure, *i.e.*, BaO- and BiO-terminations. The former one is less stable than the latter one by ~ 220 meV per slab. Hence, we only report the BiO-terminated BPTO/PbTiO₃ interface in our study.

The energy barriers between the parallel and anti-parallel states, as well as the saddle points along the transition path are found by the nudged elastic band (NEB) calculations through the climbing image NEB method [48]. In NEB calculations, a set of intermediate structures (*i.e.*, images) between the initial state (anti-parallel state) and the final state (parallel state) are generated. They are iteratively adjusted so as to minimize the increase in energy along the transition path.

The electron localization function in our study, which is used to visualize lone-pair electrons in the real space is defined as [62]:

$$\text{ELF} = \left[1 + \left(\frac{D}{D_h} \right)^2 \right]^{-1} \quad (2)$$

where

$$D = \frac{1}{2} \sum_i |\nabla \phi_i|^2 - \frac{1}{8} \frac{|\nabla \rho|^2}{\rho} \quad (3)$$

and

$$D_h = \frac{3}{10} (3\pi^2)^{\frac{5}{3}} \rho^{\frac{5}{3}} \quad (4)$$

Here ρ is the electron density and ϕ_i are the Kohn-Sham wave functions.

Crystal structure search

The crystal structure search for bulk BPTO is carried out using the particle swarm optimization algorithm implemented in CALYPSO code [11, 16], with the assistance of CrySPY [17]. More than 1000 structures (50% 10-atom $\text{BiPbTi}_2\text{O}_6$ and 50% 20-atom $\text{Bi}_2\text{Pb}_2\text{Ti}_4\text{O}_{12}$) are created in 20 generations. The structural optimization and computation of total energy are performed using VASP. In the first step of high-throughput screening of these 1000 crystal structure, we used non-spin polarized calculations with the exchange-correlation functional of PBEsol. The cutoff energy of 450 eV and the \mathbf{k} -mesh grid density is about 2000 per atom. In the second step, the lowest 50 structures are re-calculated by the spin-polarized calculations in which the cutoff energy is increased to 600 eV and the \mathbf{k} -mesh grid density is more than 2500 per atom. We consider ferromagnetic ordering and different types of antiferromagnetic orderings such as *A*-type, *C*-type and *G*-type [63] to examine possible magnetic properties. The global structure search is performed under 0 GPa. The five lowest energy structures after screening are also studied under pressure. The space groups of the predicted crystal structures are examined by the FINDSYM code [64].

Visualization

We use software VESTA to show crystal structures and real-space electron localized functions [65].

Data availability

The authors declare that all the data supporting the findings of this study are available within the paper and its Supplementary Information.

Code availability

The high-throughput crystal structural predictions were carried out using the proprietary code VASP [55, 56], with the combination of CALYPSO [11, 16] and CrySPY [17]. CALYPSO (<http://www.calypso.cn/>) is freely distributed on academic use under the license of Copyright Protection Center of China (registration No. 2010SR028200 and classifi-

ation No. 61000-7500). CrySPY (<https://github.com/Tomoki-YAMASHITA/CrySPY>) is released under the Massachusetts Institute of Technology (MIT) License and is open source. The electronic structure calculations were all performed using VASP. The thermal properties are calculated by Phonopy [66]. Phonopy (<https://github.com/atztogo/phonopy>) is released under the BSD-3-Clause License and is open source. The software VESTA [65] is distributed free of charge for academic users under the VESTA License (<https://jp-minerals.org/vesta/jp/download.html>).

Acknowledgements

We thank Kevin Garrity, Hongjun Xiang and T. Yamashita for valuable discussions. We acknowledge support from National Natural Science Foundation of China (No. 11774236), Pujiang Talents program (No. 17PJ1407300), the Seed Grants of NYU-ECNU Joint Research Institutes and the 2019 University Research Challenge Fund. This research was carried out on the High Performance Computing resources at New York University New York, Abu Dhabi and Shanghai.

Author contributions

Y.-W.F. and H.C. designed the project, performed the calculations, analyzed the results, and wrote the manuscript.

Additional information

Supplementary information accompanies the paper on the *Communications Materials* website (DOI).

Competing interests: We declare that none of the authors have competing financial or non-financial interests.

[1] Youguo Shi, Yanfeng Guo, Xia Wang, Andrew J. Princep, Dmitry Khalyavin, Pascal Manuel, Yuichi Michiue, Akira Sato, Kenji Tsuda, Shan Yu, Masao Arai, Yuichi Shirako, Masaki

- Akaogi, Nanlin Wang, Kazunari Yamaura, and Andrew T. Boothroyd, “A ferroelectric-like structural transition in a metal,” *Nat. Mater.* **12**, 1024–1027 (2013).
- [2] H. J. Xiang, “Origin of polar distortion in LiNbO₃-type “ferroelectric” metals: Role of *A*-site instability and short-range interactions,” *Phys. Rev. B* **90**, 094108 (2014).
- [3] Danilo Puggioni and James M Rondinelli, “Designing a robustly metallic noncentrosymmetric ruthenate oxide with large thermopower anisotropy,” *Nat. Commun.* **5**, 3432 (2014).
- [4] Alessio Filippetti, Vincenzo Fiorentini, Francesco Ricci, Pietro Delugas, and Jorge Íñiguez, “Prediction of a native ferroelectric metal,” *Nat. Commun.* **7**, 11211 (2016).
- [5] TH Kim, D Puggioni, Y Yuan, L Xie, H Zhou, N Campbell, PJ Ryan, Y Choi, J-W Kim, JR Patzner, S Ryu, JP Podkaminer, J Irwin, Y Ma, CJ Fennie, MS Rzchowski, XQ Pan, V Gopalan, JM Rondinelli, and CB Eom, “Polar metals by geometric design,” *Nature* **533**, 68 (2016).
- [6] Nicole A. Benedek and Turan Birol, ““ferroelectric’ metals reexamined: fundamental mechanisms and design considerations for new materials,” *J. Mater. Chem. C* **4**, 4000–4015 (2016).
- [7] Wei Luo, Ke Xu, and Hongjun Xiang, “Two-dimensional hyperferroelectric metals: A different route to ferromagnetic-ferroelectric multiferroics,” *Phys. Rev. B* **96**, 235415 (2017).
- [8] Yasuhide Mochizuki, Yu Kumagai, Hirofumi Akamatsu, and Fumiyasu Oba, “Polar metallic behavior of strained antiperovskites ACNi₃ (*A* = Mg, Zn, and Cd) from first principles,” *Phys. Rev. Materials* **2**, 125004 (2018).
- [9] Zaiyao Fei, Wenjin Zhao, Tauno A. Palomaki, Bosong Sun, Moira K. Miller, Zhiying Zhao, Jiaqiang Yan, Xiaodong Xu, and David H. Cobden, “Ferroelectric switching of a two-dimensional metal,” *Nature* **560**, 336 (2018).
- [10] Yue-Wen Fang, Hang-Chen Ding, Wen-Yi Tong, Wan-Jiao Zhu, Xin Shen, Shi-Jing Gong, Xian-Gang Wan, and Chun-Gang Duan, “First-principles studies of multiferroic and magnetoelectric materials,” *Sci. Bull.* **60**, 156–181 (2015).
- [11] Yanchao Wang, Jian Lv, Li Zhu, and Yanming Ma, “Calypso: A method for crystal structure prediction,” *Comput. Phys. Commun.* **183**, 2063–2070 (2012).
- [12] Colin W. Glass, Artem R. Oganov, and Nikolaus Hansen, “USPEX-Evolutionary crystal structure prediction,” *Comput. Phys. Commun.* **175**, 713–720 (2006).
- [13] Yingfen Wei, Pavan Nukala, Mart Salverda, Sylvia Matzen, Hong Jian Zhao, Jamo Momand, Arnoud S. Everhardt, Guillaume Agnus, Graeme R. Blake, Philippe Lecoeur, Bart J. Kooi,

- Jorge Íñiguez, Brahim Dkhil, and Beatriz Noheda, “A rhombohedral ferroelectric phase in epitaxially strained $\text{Hf}_{0.5}\text{Zr}_{0.5}\text{O}_2$ thin films,” *Nat. Mater.* **17**, 1095–1100 (2018).
- [14] Jiangang He, Yi Xia, S. Shahab Naghavi, Vidvuds Ozoliņš, and Chris Wolverton, “Designing chemical analogs to PbTe with intrinsic high band degeneracy and low lattice thermal conductivity,” *Nat. Commun.* **10**, 719 (2019).
- [15] Ziyuan Zhao, Shoutao Zhang, Tong Yu, Haiyang Xu, Aitor Bergara, and Guochun Yang, “Predicted pressure-induced superconducting transition in electride Li_6P ,” *Phys. Rev. Lett.* **122**, 097002 (2019).
- [16] Yanchao Wang, Jian Lv, Li Zhu, and Yanming Ma, “Crystal structure prediction via particle-swarm optimization,” *Phys. Rev. B* **82**, 094116 (2010).
- [17] Tomoki Yamashita, Nobuya Sato, Hiori Kino, Takashi Miyake, Koji Tsuda, and Tamio Oguchi, “Crystal structure prediction accelerated by bayesian optimization,” *Phys. Rev. Materials* **2**, 013803 (2018).
- [18] Motohiko Murakami, Kei Hirose, Katsuyuki Kawamura, Nagayoshi Sata, and Yasuo Ohishi, “Post-perovskite phase transition in mgsiO_3 ,” *Science* **304**, 855–858 (2004).
- [19] Kenji Ohta, Suzue Onoda, Kei Hirose, Ryosuke Sinmyo, Katsuya Shimizu, Nagayoshi Sata, Yasuo Ohishi, and Akira Yasuhara, “The electrical conductivity of post-perovskite in earth’s D” layer,” *Science* **320**, 89–91 (2008).
- [20] Abhijit Biswas, Chan-Ho Yang, Ramamoorthy Ramesh, and Yoon H. Jeong, “Atomically flat single terminated oxide substrate surfaces,” *Prog. Surf. Sci.* **92**, 117–141 (2017).
- [21] Zhihong Zhang, Kurt Leinenweber, Matt Bauer, Laurence A. J. Garvie, Paul F. McMillan, and George H. Wolf, “High-pressure bulk synthesis of crystalline $\text{C}_6\text{N}_9\text{H}_3\cdot\text{HCl}$: a novel C_3N_4 graphitic derivative,” *J. Am. Chem. Soc.* **123**, 7788–7796 (2001).
- [22] R. A. Klein, A. B. Altman, R. J. Saballos, J. P. S. Walsh, A. D. Tamerius, Y. Meng, D. Puggioni, S. D. Jacobsen, J. M. Rondinelli, and D. E. Freedman, “High-pressure synthesis of the BiVO_3 perovskite,” *Phys. Rev. Mater.* **3**, 064411 (2019).
- [23] Ghenadii Korotcenkov, *Metal Oxide-based Thin Film Structures: Formation, Characterization and Application of Interface-based Phenomena* (Elsevier, , 2017).
- [24] Esteban I Paredes Aulesti, Yiu Wing Cheung, Yue-Wen Fang, Jianfeng He, Kazunari Yamaura, Kwing To Lai, Swee K Goh, and Hanghui Chen, “Pressure-induced enhancement of non-polar to polar transition temperature in metallic LiOsO_3 ,” *Appl. Phys. Lett.* **113**, 12902

- (2018).
- [25] Rossitza Pentcheva and Warren E. Pickett, “Correlation-driven charge order at the interface between a mott and a band insulator,” *Phys. Rev. Lett.* **99**, 016802 (2007).
 - [26] E. Pavarini, S. Biermann, A. Poteryaev, A. I. Lichtenstein, A. Georges, and O. K. Andersen, “Mott transition and suppression of orbital fluctuations in orthorhombic $3d^1$ perovskites,” *Phys. Rev. Lett.* **92**, 176403 (2004).
 - [27] Patrick Fazekas, *Lecture notes on electron correlation and magnetism* (World scientific, , 1999).
 - [28] Karolina Janicka, Julian P. Velev, and Evgeny Y. Tsymbal, “Magnetism of $\text{LaAlO}_3/\text{SrTiO}_3$ superlattices,” *J. Appl. Phys.* **103**, 07B508 (2008).
 - [29] Ronald E Cohen, “Origin of ferroelectricity in perovskite oxides,” *Nature* **358**, 136 (1992).
 - [30] P. Ravindran, R. Vidya, A. Kjekshus, H. Fjellvåg, and O. Eriksson, “Theoretical investigation of magnetoelectric behavior in BiFeO_3 ,” *Phys. Rev. B* **74**, 224412 (2006).
 - [31] Wei Luo and Hongjun Xiang, “Two-dimensional phosphorus oxides as energy and information materials,” *Angewandte Chemie* **128**, 8717–8722 (2016).
 - [32] Hong Jian Zhao, Alessio Filippetti, Carlos Escorihuela-Sayalero, Pietro Delugas, Enric Canadell, L. Bellaiche, Vincenzo Fiorentini, and Jorge Íñiguez, “Meta-screening and permanence of polar distortion in metallized ferroelectrics,” *Phys. Rev. B* **97**, 054107 (2018).
 - [33] Jun-xing Gu, Kui-juan Jin, Chao Ma, Qing-hua Zhang, Lin Gu, Chen Ge, Jie-su Wang, Can Wang, Hai-zhong Guo, and Guo-zhen Yang, “Coexistence of polar distortion and metallicity in $\text{PbTi}_{1-x}\text{Nb}_x\text{O}_3$,” *Phys. Rev. B* **96**, 165206 (2017).
 - [34] Xu He and Kui-juan Jin, “Persistence of polar distortion with electron doping in lone-pair driven ferroelectrics,” *Phys. Rev. B* **94**, 224107 (2016).
 - [35] Xin-Wei Shen, Yue-Wen Fang, Bo-Bo Tian, and Chun-Gang Duan, “Two-dimensional ferroelectric tunnel junction: the case of monolayer $\text{In:SnSe/SnSe/Sb:SnSe}$ homostructure,” *ACS Appl. Electron. Mater.* **1**, 1133–1140 (2019).
 - [36] Pio Baettig, Ram Seshadri, and Nicola A Spaldin, “Anti-polarity in ideal BiMnO_3 ,” *J. Am. Chem. Soc.* **129**, 9854–9855 (2007).
 - [37] V Goian, S Kamba, M Savinov, D Nuzhnyy, F Borodavka, P Vaněk, and AA Belik, “Absence of ferroelectricity in BiMnO_3 ceramics,” *J. Appl. Phys.* **112**, 074112 (2012).
 - [38] Ram Seshadri and Nicola A. Hill, “Visualizing the role of Bi $6s$ lone pairs in the off-center distortion in ferromagnetic BiMnO_3 ,” *Chem. Mater.* **13**, 2892–2899 (2001).

- [39] P. W. Anderson and E. I. Blount, “Symmetry considerations on martensitic transformations: “ferroelectric” metals?” *Phys. Rev. Lett.* **14**, 217 (1965).
- [40] Jacek C. Wojdeł and Jorge Íñiguez, “Testing simple predictors for the temperature of a structural phase transition,” *Phys. Rev. B* **90**, 014105 (2014).
- [41] Yong Wang, Xiaohui Liu, J. D. Burton, Sitaram S. Jaswal, and Evgeny Y. Tsymbal, “Ferroelectric instability under screened coulomb interactions,” *Phys. Rev. Lett.* **109**, 247601 (2012).
- [42] Chengliang Xia, Yue Chen, and Hanghui Chen, “Coexistence of polar displacements and conduction in doped ferroelectrics: An ab initio comparative study,” *Phys. Rev. Mater.* **3**, 054405 (2019).
- [43] Danilo Puggioni, Gianluca Giovannetti, and James M. Rondinelli, “Polar metals as electrodes to suppress the critical-thickness limit in ferroelectric nanocapacitors,” *J. Appl. Phys* **124**, 174102 (2018).
- [44] Danilo Puggioni, Gianluca Giovannetti, Massimo Capone, and James M. Rondinelli, “Design of a mott multiferroic from a nonmagnetic polar metal,” *Phys. Rev. Lett.* **115**, 087202 (2015).
- [45] Yi Zhang, Lin Xie, Jeongwoo Kim, Alex Stern, Hui Wang, Kui Zhang, Xingxu Yan, Linze Li, Henry Liu, Gejian Zhao, Hang Chi, Chaitanya Gadre, Qiyin Lin, Yichun Zhou, Ctirad Uher, Tingyong Chen, Ying-Hao Chu, Jing Xia, Ruqian Wu, and Xiaoqing Pan, “Discovery of a magnetic conductive interface in $\text{PbZr}_{0.2}\text{Ti}_{0.8}\text{O}_3/\text{SrTiO}_3$ heterostructures,” *Nat. Commun.* **9**, 685 (2018).
- [46] Menglei Li, Yijia Gu, Yi Wang, Long-Qing Chen, and Wenhui Duan, “First-principles study of 180° domain walls in BaTiO_3 : Mixed Bloch-Néel-Ising character,” *Phys. Rev. B* **90**, 054106 (2014).
- [47] B. Meyer and David Vanderbilt, “Ab initio study of ferroelectric domain walls in PbTiO_3 ,” *Phys. Rev. B* **65**, 104111 (2002).
- [48] Graeme Henkelman, Blas P. Uberuaga, and Hannes Jansson, “A climbing image nudged elastic band method for finding saddle points and minimum energy paths,” *J. Chem. Phys.* **113**, 9901–9904 (2000).
- [49] Keith J. Laidler and M. Christine King, “Development of transition-state theory,” *J. Phys. Chem.* **87**, 2657–2664 (1983).
- [50] E.B. Tadmor, U.V. Waghmare, G.S. Smith, and E. Kaxiras, “Polarization switching in PbTiO_3 : an ab initio finite element simulation,” *Acta Mater.* **50**, 2989–3002 (2002).

- [51] Hua Wang and Xiaofeng Qian, “Two-dimensional multiferroics in monolayer group IV monochalcogenides,” *2D Mater.* **4**, 015042 (2017).
- [52] X. Y. Li, Q. Yang, J. X. Cao, L. Z. Sun, Q. X. Peng, Y. C. Zhou, and R. X. Zhang, “Domain wall motion in perovskite ferroelectrics studied by the nudged elastic band method,” *J. Phys. Chem. C* **122**, 3091–3100 (2018).
- [53] At room temperature, $1 k_B T \approx 26$ meV. In transition state theory, the probability P of overcoming the energy barrier is proportional to $e^{-\Delta E/k_B T}$, *i.e.*, $P \propto e^{-\Delta E/k_B T}$. The energy barrier ($\Delta E = 58$ meV) is about twice the $k_B T$, hence the probability of overcoming this barrier is around 14%.
- [54] P. E. Blöchl, “Projector augmented-wave method,” *Phys. Rev. B* **50**, 17953–17979 (1994).
- [55] G. Kresse and J. Furthmüller, “Efficiency of ab-initio total energy calculations for metals and semiconductors using a plane-wave basis set,” *Comp. Mater. Sci.* **6**, 15–50 (1996).
- [56] G. Kresse and J. Furthmüller, “Efficient iterative schemes for ab initio total-energy calculations using a plane-wave basis set,” *Phys. Rev. B* **54**, 11169–11186 (1996).
- [57] John P. Perdew, Adrienn Ruzsinszky, Gábor I. Csonka, Oleg A. Vydrov, Gustavo E. Scuseria, Lucian A. Constantin, Xiaolan Zhou, and Kieron Burke, “Restoring the density-gradient expansion for exchange in solids and surfaces,” *Phys. Rev. Lett.* **100**, 136406 (2008).
- [58] S. L. Dudarev, G. A. Botton, S. Y. Savrasov, C. J. Humphreys, and A. P. Sutton, “Electron-energy-loss spectra and the structural stability of nickel oxide: An LSDA+U study,” *Phys. Rev. B* **57**, 1505–1509 (1998).
- [59] Gianluca Giovannetti and Massimo Capone, “Dual nature of the ferroelectric and metallic state in LiOsO_3 ,” *Phys. Rev. B* **90**, 195113 (2014).
- [60] G. Makov and M. C. Payne, “Periodic boundary conditions in ab initio calculations,” *Phys. Rev. B* **51**, 4014–4022 (1995).
- [61] Jörg Neugebauer and Matthias Scheffler, “Adsorbate-substrate and adsorbate-adsorbate interactions of Na and K adlayers on $\text{Al}(111)$,” *Phys. Rev. B* **46**, 16067–16080 (1992).
- [62] Bernard Silvi and Andreas Savin, “Classification of chemical bonds based on topological analysis of electron localization functions,” *Nature* **371**, 683 (1994).
- [63] Hang-Chen Ding and Chun-Gang Duan, “Electric-field control of magnetic ordering in the tetragonal-like BiFeO_3 ,” *EPL (Europhys. Lett.)* **97**, 57007 (2012).
- [64] Mois I Aroyo, JM Perez-Mato, D Orobengoa, E Tasci, G De La Flor, and A Kirov, “Crystal-

- lography online: Bilbao crystallographic server,” *Bulg. Chem. Commun* **43**, 183–197 (2011).
- [65] Koichi Momma and Fujio Izumi, “VESTA 3 for three-dimensional visualization of crystal, volumetric and morphology data,” *J. Appl. Crystallogr.* **44**, 1272–1276 (2011).
- [66] Atsushi Togo and Isao Tanaka, “First principles phonon calculations in materials science,” *Scr. Mater.* **108**, 1–5 (2015).

Supplementary Information for:
Design of a multifunctional polar metal via first-principles
high-throughput structure screening

Yue-Wen Fang^{1,2*} and Hanghui Chen^{2,3†}

¹*Department of Materials Science and Engineering, Kyoto University, Kyoto, Japan*

²*NYU-ECNU Institute of Physics, New York University Shanghai China*

³*Department of Physics, New York University, New York 10003, USA*

(Dated: February 6, 2020)

* fyuwen@gmail.com

† hanghui.chen@nyu.edu

Supplementary Note 1. Low-energy structures predicted from CALYPSO search

Supplementary Table 1. A list of predicted crystal structures including ten lowest energy states, perovskite anti-polar state with $Pmma$ symmetry, and post-perovskite anti-polar state with $Pmmm$ symmetry. ‘—’ represents non-perovskite and non-post-perovskite structures. Post-perovskite structures are explicitly shown. ‘Layered’, ‘Rock-salt’, and ‘Columnar’ refer to different cation orderings of A -site ordered double perovskite structure (the naming convention follows Ref. [1]).

Phase	Cell parameters	Atom type	Wyckoff site	X	Y	Z	Ordering	E (meV)
$Pmm2$	$a = 5.616 \text{ \AA}$	Ti1	2g	0.483	0.251	0.000	Post-perovskite 0	
		Bi1	1c	-0.074	0.000	0.500		
	$b = 3.035 \text{ \AA}$	Pb1	1d	0.018	0.500	0.500		
		O1	2h	0.264	0.216	0.500		
	$c = 7.597 \text{ \AA}$	O2	2h	0.724	0.270	0.500		
	$\alpha = 90.000^\circ$	O3	1a	0.575	0.000	0.000		
	$\beta = 90.000^\circ$	O4	1b	0.439	0.500	0.000		
	$\gamma = 90.000^\circ$							
$Pmn2_1$	$a = 5.520 \text{ \AA}$	Ti1	4b	0.056	0.742	0.749	Rock-salt	93.0
		Bi1	2a	0.517	0.785	0.000		
	$b = 5.543 \text{ \AA}$	Pb1	2a	0.039	0.258	0.000		
		O1	4b	0.279	0.463	0.736		
	$c = 7.993 \text{ \AA}$	O2	4b	0.860	0.045	0.746		
	$\alpha = 90.000^\circ$	O3	2a	0.099	0.750	0.000		
	$\beta = 90.000^\circ$	O4	2b	0.557	0.221	0.000		
	$\gamma = 90.000^\circ$							
$Pmm2$	$a = 4.077 \text{ \AA}$	Ti1	2g	0.542	0.000	0.245	Layered	93.2
		Bi1	1d	0.129	0.500	0.500		
	$b = 3.919 \text{ \AA}$	Pb1	1c	0.079	0.500	0.000		
		O1	2g	-0.014	0.000	0.253		
	$c = 7.887 \text{ \AA}$	O2	2h	0.457	0.500	0.259		
	$\alpha = 90.000^\circ$	O3	1a	0.480	0.000	0.000		
	$\beta = 90.000^\circ$	O4	1b	0.441	0.000	0.500		
	$\gamma = 90.000^\circ$							

		Ti1	1a	0.312	0.738	0.155		
		Ti2	1a	0.425	0.835	0.381		
		Ti3	1a	0.621	0.175	0.768		
		Ti4	1a	0.719	0.710	-0.033		
		Bi1	1a	0.014	0.244	0.538		
		Bi2	1a	0.044	0.768	0.617		
		Pb1	1a	0.221	0.216	-0.030		
	$a = 3.743 \text{ \AA}$	Pb2	1a	0.865	0.252	0.286		
	$b = 5.943 \text{ \AA}$	O1	1a	0.136	0.189	0.797		
$P1$	$c = 13.435 \text{ \AA}$	O2	1a	0.237	0.735	0.002	—	103.4
	$\alpha = 93.478^\circ$	O3	1a	0.336	0.024	0.200		
	$\beta = 97.928^\circ$	O4	1a	0.371	0.587	0.271		
	$\gamma = 90.068^\circ$	O5	1a	0.451	0.161	0.423		
		O6	1a	0.485	0.706	0.498		
		O7	1a	0.563	0.314	0.649		
		O8	1a	0.590	0.884	0.708		
		O9	1a	0.682	0.450	0.891		
		O10	1a	0.694	-0.009	-0.085		
		O11	1a	0.793	0.665	0.115		
		O12	1a	-0.086	0.883	0.356		
	$a = 5.561 \text{ \AA}$	Ti1	4b	0.000	0.500	0.216		
	$b = 5.561 \text{ \AA}$	Bi1	2a	0.000	0.000	0.508		
$I4mm$	$c = 8.161 \text{ \AA}$	Pb1	2a	0.000	0.000	-0.016	Rock-salt	109.1
	$\alpha = 90.000^\circ$	O1	8c	0.743	0.743	0.173		
	$\beta = 90.000^\circ$	O2	4b	0.000	0.500	0.437		
	$\gamma = 90.000^\circ$							

<i>Cm</i>	$a = 7.923 \text{ \AA}$	Ti1	4b	0.465	0.257	0.060	Columnar	120.0
	$b = 7.875 \text{ \AA}$	Bi1	2a	0.667	0.000	0.622		
	$c = 3.972 \text{ \AA}$	Pb1	2a	0.201	0.000	0.577		
	$\alpha = 90.000^\circ$	O1	4b	0.224	0.285	0.036		
	$\beta = 90.000^\circ$	O2	4b	0.484	0.245	0.551		
	$\gamma = 90.000^\circ$	O3	2a	0.006	0.000	0.051		
		O4	2b	0.460	0.000	0.031		
<i>R32</i>	$a = 5.475 \text{ \AA}$	Ti1	6c	0.000	0.000	0.747	Rock-salt	137.3
	$b = 5.475 \text{ \AA}$	Bi1	3b	0.000	0.000	0.500		
	$c = 5.475 \text{ \AA}$	Pb1	3a	0.000	0.000	0.000		
	$\alpha = 61.727^\circ$	O1	9d	0.449	0.000	0.000		
	$\beta = 61.727^\circ$	O2	9e	0.573	0.000	0.500		
	$\gamma = 61.727^\circ$							
<i>P2₁2₁2</i>	$a = 5.494 \text{ \AA}$	Ti1	4c	0.501	0.750	0.252	Rock-salt	138.3
	$b = 7.980 \text{ \AA}$	Bi1	2b	0.000	0.500	0.233		
	$c = 5.498 \text{ \AA}$	Pb1	2a	0.000	0.000	0.253		
	$\alpha = 90.000^\circ$	O1	4c	0.699	0.239	0.548		
	$\beta = 90.000^\circ$	O2	4c	0.704	0.759	-0.048		
	$\gamma = 90.000^\circ$	O3	2a	0.000	0.000	0.749		
		O4	2b	0.000	0.500	0.764		
<i>I4₂m</i>	$a = 5.492 \text{ \AA}$	Ti1	4d	0.000	0.500	0.250	Rock-salt	139.4
	$b = 5.492 \text{ \AA}$	Bi1	2b	0.000	0.000	0.500		
	$c = 5.569 \text{ \AA}$	Pb1	2a	0.000	0.000	0.000		
	$\alpha = 119.545^\circ$	O1	8i	0.201	0.201	0.260		
	$\beta = 119.545^\circ$	O2	4c	0.000	0.500	0.000		
	$\gamma = 90.000^\circ$							

<i>Pnmm</i>	$a = 5.4916 \text{ \AA}$	Ba1	2b	0.000	0.000	0.500	Rock-salt	135.0
	$b = 5.4915 \text{ \AA}$	Pb1	2a	0.000	0.000	0.000		
	$c = 7.9943 \text{ \AA}$	Ti1	4f	0.000	0.500	0.750		
	$\alpha = 90.000^\circ$	O1	8h	0.7024	0.70239	0.761		
	$\beta = 90.000^\circ$	O2	2c	0.000	0.500	0.000		
	$\gamma = 90.000^\circ$	O3	2d	0.000	0.500	0.500		
<i>Pmma</i>	$a = 3.945 \text{ \AA}$	Ti1	4j	0.500	0.492	0.378	Layered	158.0
	$b = 3.951 \text{ \AA}$	Bi1	2e	0.000	0.882	0.250		
	$c = 15.859 \text{ \AA}$	Pb1	2a	0.000	0.000	0.000		
	$\alpha = 90.000^\circ$	O1	2d	0.500	0.500	0.000		
	$\beta = 90.000^\circ$	O2	4j	0.500	0.012	0.126		
	$\gamma = 90.000^\circ$	O3	4i	0.000	0.531	0.131		
		O4	2f	0.500	0.553	0.250		
<i>Pmmm</i>	$a = 3.057 \text{ \AA}$	Bi1	1b	0.500	0.000	0.000	Post-perovskite	218.5
	$b = 7.637 \text{ \AA}$	Pb1	1f	0.500	0.500	0.000		
	$c = 5.539 \text{ \AA}$	Ti1	2n	0.000	0.249	0.500		
	$\alpha = 90.000^\circ$	O1	4v	0.500	0.242	0.263		
	$\beta = 90.000^\circ$	O2	1c	0.000	0.000	0.500		
	$\gamma = 90.000^\circ$	O3	1g	0.000	0.500	0.500		

In our structure search, we consider all possible cation orderings in perovskite structure, as well as non-perovskite structures such as post-perovskite and hexagonal structures.

Supplementary Table I lists twelve crystal structures of $\text{BiPbTi}_2\text{O}_6$, including ten lowest energy structures predicted by CALYPSO, perovskite anti-polar structure with *Pmma* symmetry and post-perovskite anti-polar structure with *Pmmm* symmetry. All the energies in Supplementary Table I are normalized to per formula unit (*i.e.*, 10-atom $\text{BiPbTi}_2\text{O}_6$). The total energy of post-perovskite *Pmm2* structure (the one with the lowest energy) is set as the zero point.

Supplementary Note 2. Structural information of available substrates

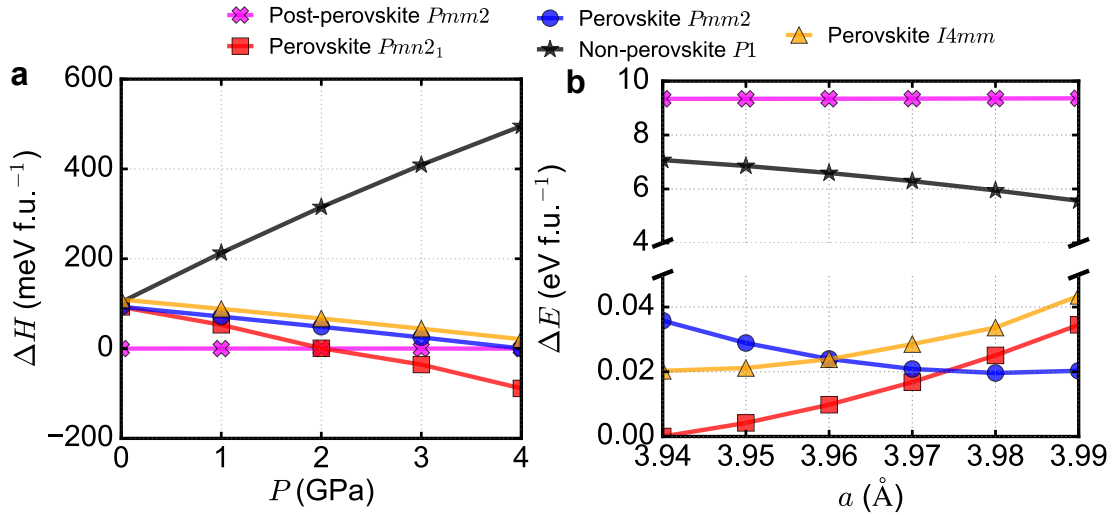
Supplementary Table 2. Structural information of perovskite oxide substrates KTaO_3 and NdScO_3 , calculated by DFT-PBEsol method. The experimental lattice constants, taken from Ref. [2] are also shown in the parentheses for comparison.

Substrate	Cell parameters	Atom type	Wyckoff site	X	Y	Z
KTaO_3	$a = 4.001$ (3.988) Å					
	$b = 4.001$ (3.988) Å					
	$c = 4.001$ (3.988) Å	K1	1b	0.500	0.500	0.500
	$\alpha = 90.000^\circ$	Ta1	1a	0.000	0.000	0.000
	$\beta = 90.000^\circ$	O1	3d	0.500	0.000	0.000
	$\gamma = 90.000^\circ$					
NdScO_3	$a = 5.496$ (5.57) Å					
	$b = 5.752$ (5.77) Å	Nd1	4c	0.250	0.482	0.437
	$c = 7.886$ (7.99) Å	Sc1	4b	0.000	0.500	0.000
	$\alpha = 90.000^\circ$	O1	8d	0.062	0.192	0.194
	$\beta = 90.000^\circ$	O2	4c	0.250	0.623	0.048
	$\gamma = 90.000^\circ$					

We study two perovskite oxide substrates KTaO_3 and NdScO_3 [2]. As shown in Supplementary Table II, the DFT (PBEsol) calculated lattice constants of KTaO_3 and NdScO_3 are in good agreement with the experimental lattice constants (within 1% difference). We find that cubic perovskite KTaO_3 (cubic lattice constant of ~ 4.00 Å) and orthorhombic perovskite NdScO_3 (pseudo-cubic lattice constant of ~ 4.08 Å) can impose tensile strain sufficiently to stabilize perovskite $Pmm2$ $\text{BiPbTi}_2\text{O}_6$ in thin film form. In our main text, the heterostructure of $\text{BiPbTi}_2\text{O}_6/\text{PbTiO}_3$ is simulated to growth on the substrate of KTaO_3 .

Supplementary Note 3. Pressure and strain study including $P1$ and $I4mm$ structures

In this section, we study more crystal structures under pressure and strain. We consider not only the three lowest energy structures (post-perovskite $Pmm2$, perovskite $Pmn2_1$ and perovskite $Pmm2$), but also the other two low-energy structures (a non-perovskite $P1$ and perovskite $I4mm$). Panel **a** of Supplementary Figure 1 shows the pressure dependence and panel **b** of Supplementary Figure 1 shows the strain dependence. The conclusion in the main text does not change after we consider more low-energy structures.



Supplementary Figure 1. **Pressure and strain study on post-perovskite $Pmm2$, perovskite $Pmn2_1$, perovskite $Pmm2$, non-perovskite $P1$, and perovskite $I4mm$ structures.** Panel **a** shows the enthalpy difference ΔH as a function of pressure. The enthalpy of post-perovskite $Pmm2$ structure under each pressure is set as zero point. ΔE has the unit of meV f.u.⁻¹. Panel **b** shows the energy difference ΔE as a function of epitaxial strain. The energy of perovskite $Pmn2_1$ with in-plane lattice constant of 3.94 Å is set as zero point. Note that we use a broken y -axis for ΔE . In the top half y -axis, the energy runs from 4 to 10 eV f.u.⁻¹; in the bottom y -axis, the energy ranges from 0 to 0.04 eV f.u.⁻¹. The magenta, red, blue, black, and orange curves correspond to post-perovskite $Pmm2$, perovskite $Pmn2_1$, perovskite $Pmm2$, non-perovskite $P1$, and perovskite $I4mm$ structures, respectively.

Supplementary Note 4. Temperature effect on the phase transitions

In order to investigate the temperature effect on the phase transitions between post-perovskite $Pmm2$, perovskite $Pmn2_1$ and perovskite $Pmm2$, we study the Helmholtz free energies of the three phases.

The Helmholtz free energy for a defect-free non-magnetic system with atomic volume V at temperature T can be approximated as [3–5]

$$F(V, T) = F_{\text{ph}}(V, T) + F_{\text{ele}}(V, T), \quad (1)$$

where $F_{\text{ph}}(V, T)$ is the phonon free energy (*i.e.*, vibrational free energy) and $F_{\text{ele}}(V, T)$ is the thermal electron contribution to the free energy.

The electron free energy $F_{\text{ele}}(V, T)$ can be divided into the total energy E_0 at 0 K and the remaining part $\bar{F}_{\text{ele}}(V, T)$ [6]:

$$F_{\text{ele}}(V, T) = E_0 + \bar{F}_{\text{ele}}(V, T). \quad (2)$$

E_0 can be calculated by standard density functional theory (DFT). In quasi-harmonic approximation, $\bar{F}_{\text{ele}}(V, T)$ can be calculated by using Mermin's finite temperature formulation of DFT [6, 7], but requires very large supercell calculations (for BPTO, the supercells need to contain 160~320 atoms) with a range of volumes under the studied temperatures.

However, at elevated temperatures, when studying structural transitions, phonon entropy plays a much more important role than electron entropy [8]. Phonon free energy F_{ph} can be readily calculated by using density functional perturbation theory or frozen phonon method [9, 10].

Therefore we approximate $F_{\text{ele}}(V, T)$ as the zero-temperature total energy E_0 [9, 10]. Furthermore we notice that thermal expansion in solids is usually small and thus we use the volume of the zero-temperature crystal structures. Thus, the Helmholtz free energy in Equation (1) is approximated as

$$F(V, T) \simeq E_0 + F_{\text{ph}}(T). \quad (3)$$

The phonon free energy $F_{\text{ph}}(T)$ is defined as

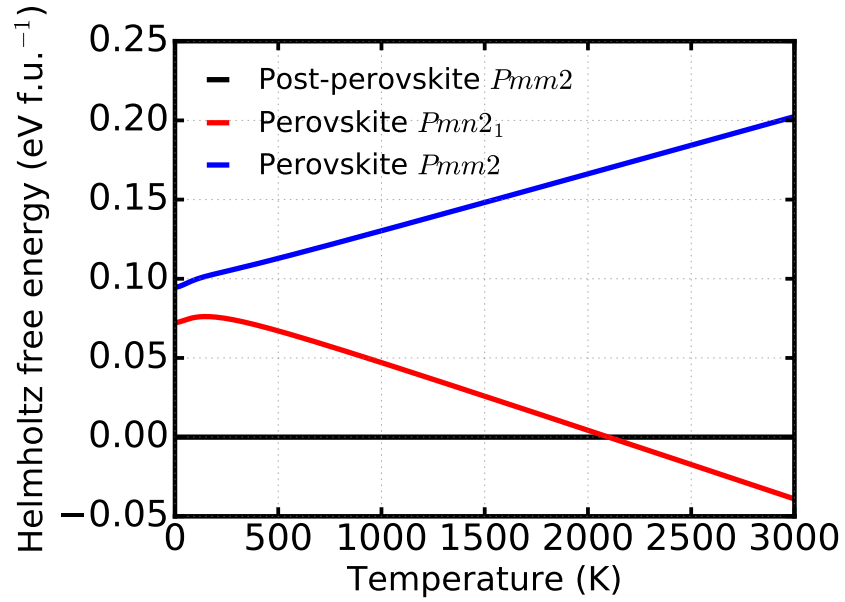
$$F_{\text{ph}}(T) = E_{\text{ph}}(T) - TS_{\text{ph}}(T), \quad (4)$$

where $E_{\text{ph}}(T)$ is the phonon energy and $S_{\text{ph}}(T)$ is the phonon entropy, both at the volume of zero-temperature crystal structure. More specifically, the phonon Helmholtz free energy $F_{\text{ph}}(T)$ can be calculated from the phonon frequencies by [9]

$$F_{\text{ph}} = \frac{1}{2} \sum_{\mathbf{q}j} \hbar\omega_{\mathbf{q}j} + k_B T \sum_{\mathbf{q}j} \ln[1 - \exp(-\hbar\omega_{\mathbf{q}j}/k_B T)], \quad (5)$$

where \mathbf{q} , j , ω , T , and k_B are wave vector, band index of phonon dispersions, phonon frequency, temperature, and Boltzmann constant, respectively. In our study, the phonon frequencies are calculated by combining first-principles calculations with the supercell method and finite displacement method implemented in Phonopy [9]. The dimensions of supercells of the $Pmm2$ post-perovskite, $Pmm2$ perovskite, and $Pmn2_1$ perovskite are $4 \times 2 \times 4$ (320 atoms), $3 \times 2 \times 3$ (180 atoms), and $2 \times 2 \times 2$ (160 atoms) of their unit cells, respectively. The corresponding \mathbf{k} -mesh for DFT calculations of the supercells of $Pmm2$ post-perovskite, $Pmm2$ perovskite, and $Pmn2_1$ perovskite are $8 \times 6 \times 6$, $5 \times 3 \times 5$, and $8 \times 3 \times 7$, respectively.

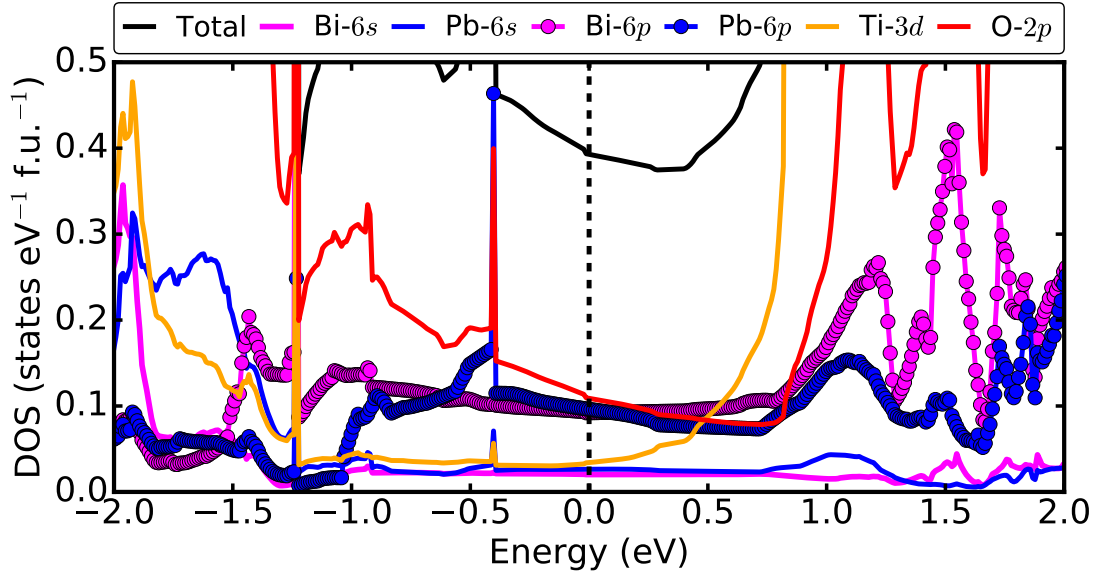
The obtained Helmholtz free energy $F(T) = E_0 + F_{\text{ph}}(T)$ as a function of temperature (up to 3000 K) is shown in Supplementary Figure 2. Under 2100 K, the post-perovskite $Pmm2$ is the most stable phase. There is a phase transition between the post-perovskite $Pmm2$ and the perovskite $Pmn2_1$ around 2100 K, hence the perovskite $Pmn2_1$ becomes the most stable one above 2100 K.



Supplementary Figure 2. The approximate Helmholtz free energy Eq. (4) of post-perovskite $Pmm2$ (horizontal black line), perovskite $Pmm2$ (blue line) and perovskite $Pmn2_1$ (red line). The Helmholtz free energy of post-perovskite $Pmm2$ is set as the zero point.

Supplementary Note 5. The DOS of post-perovskite $pmm2$ structure

Supplementary Figure 3 shows the total density of states (DOS) and orbital projected densities of states of post-perovskite $Pmm2$ $\text{BiPbTi}_2\text{O}_6$. The DOS at the Fermi level is mainly composed of O-2p, Bi-6p and Pb-6p states, with very small contributions from Ti-3d, Bi-6s and Pb-6s states.

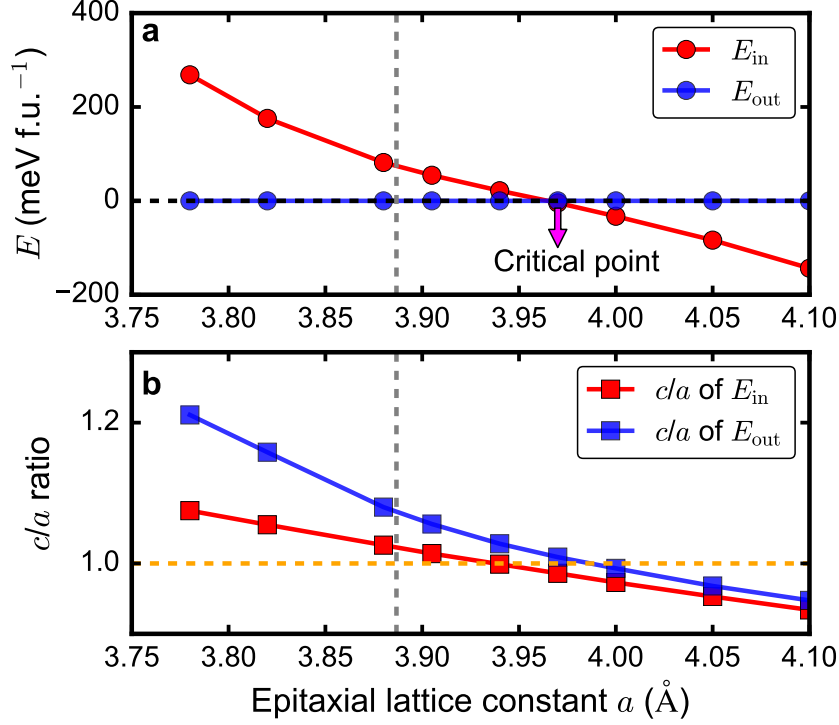


Supplementary Figure 3. **The density of states of $Pmm2$ $\text{BiPbTi}_2\text{O}_6$.** The black curve is the total DOS. The magenta curve, magenta curve with circle markers, blue curve, blue curve with circle markers, orange curve and red curve are Bi-6s, Bi-6p, Pb-6s, Pb-6p, Ti-3d and O-2p projected DOS, respectively. The dashed line is the Fermi level.

Supplementary Note 6. PbTiO_3 under bi-axial strain

In experiment, bulk PbTiO_3 displays a spontaneous polarization of about 0.75 C/m^2 at 295 K with c/a ratio of 1.063 and space group of $P4mm$ [11, 12]. In this section, we use first-principles calculations (DFT-PBEsol) to study PbTiO_3 under bi-axial strain. In structural optimizations, we use an energy cutoff of 600 eV and \mathbf{k} mesh of $17 \times 17 \times 17$. The convergence thresholds of energy and atomic Hellmann-Feynman forces are 10^{-9} eV and 10^{-4} eV \AA^{-1} , respectively. We fix the in-plane epitaxial lattice constants ($a_x = a_y = a$) and allow the out-of-plane lattice constant $a_z = c$ to change. All the internal atomic coordinates are fully relaxed. We study two different polarization orientations: if the polarization is along z -axis, the state is referred to as “out-of-plane polarization”; if the polarization is either along x -axis or y -axis, the state is referred to as “in-plane polarization”.

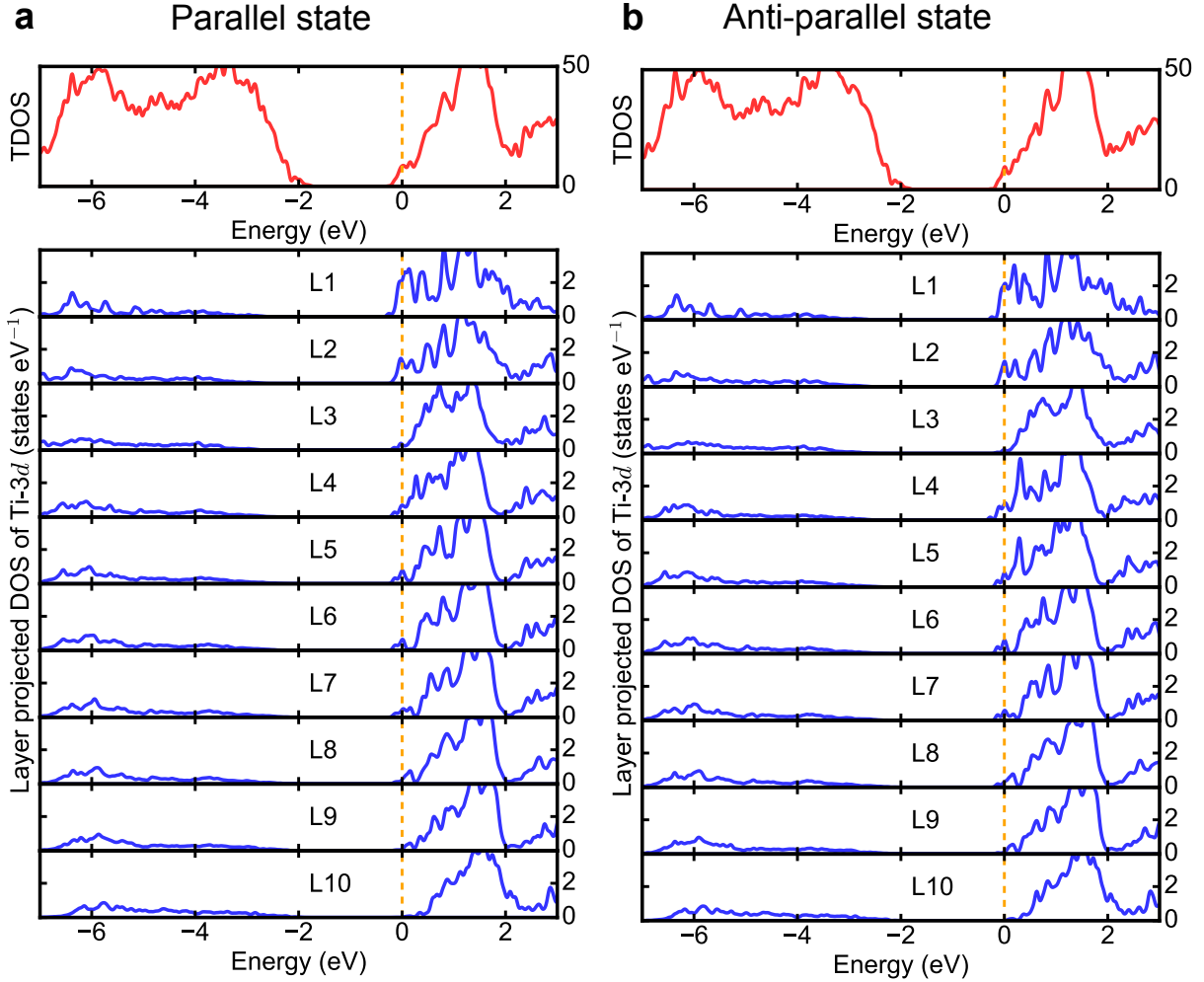
We change the in-plane epitaxial lattice constant a and study the energy difference between the “out-of-plane polarization” and the “in-plane polarization” states as a function of a . The results are shown in Supplementary Figure 4a. There is a critical lattice constant $a_c \simeq 3.97 \text{ \AA}$ at which the two states are degenerate. If the epitaxial lattice constant is less than a_c , the “out-of-plane polarization” state is more energetically favorable. If the epitaxial lattice constant exceeds a_c , the “in-plane polarization” state becomes more stable. Supplementary Figure 4b shows the c/a ratio of both “out-of-plane polarization” and “in-plane polarization” states as a function of the in-plane epitaxial lattice constant a . We note that without any strain, our calculations find that bulk PbTiO_3 has lattice constants $a_x = a_y = 3.89 \text{ \AA}$ and $a_z = 4.17 \text{ \AA}$ with its polarization pointing along z axis. This indicates that if we want to stabilize an in-plane polarization in PbTiO_3 thin films, we need at least 2% bi-axial tensile strain.



Supplementary Figure 4. **PbTiO₃ under bi-axial strain.** Panel **a**: total energies of “in-plane polarization” state (E_{in}) and “out-of-plane polarization” state (E_{out}) of PbTiO₃ under bi-axial strain. For each given epitaxial lattice constant a , E_{out} is chosen as the zero energy. At $a = 3.97$ Å, the two states are degenerate. When $a < 3.97$ Å, the “out-of-plane polarization” state is more energetically favorable. When $a > 3.97$ Å, the “in-plane polarization” state is more stable. Panel **b**: the c/a ratio of both “in-plane polarization” state and “out-of-plane polarization” state as a function of epitaxial lattice constant a . In both panels, the grey dashed line refers to strain-free PbTiO₃ which has theoretical lattice constants $a_x = a_y = 3.89$ Å and $a_z = 4.17$ Å.

Supplementary Note 7. Density of states of BiPbTiO₆/PbTiO₃ interface

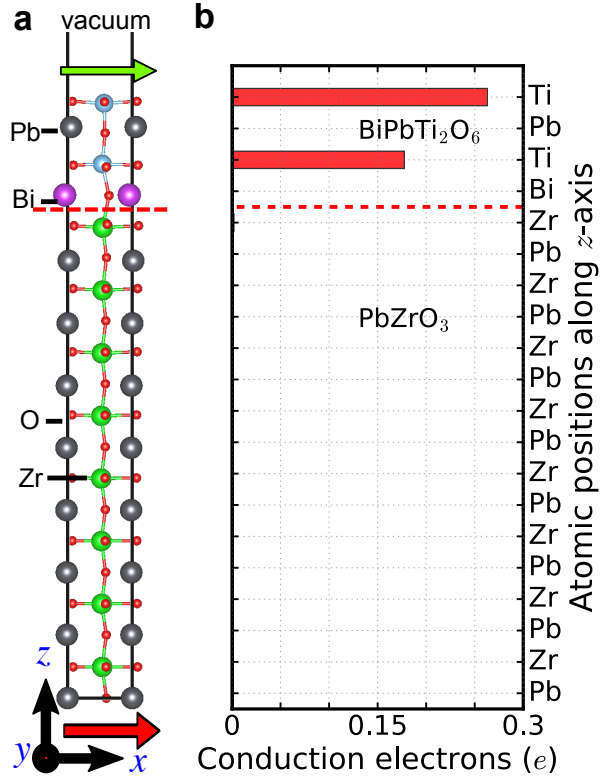
Total density of states and layer-resolved density of states projected onto Ti-3d orbitals for both parallel and anti-parallel states are shown in Supplementary Figure 5. The layer-resolved conduction electrons in the main text are calculated by integrating the partial density states of Ti-3d orbitals.



Supplementary Figure 5. **Total density of states (TDOS) and the layer-resolved density of states projected onto Ti-3d orbitals (layer projected DOS).** Panel a: parallel state. Panel b: anti-parallel state. Red and blue curves correspond to TDOS and layer projected DOS, respectively. L1...L10 refer to the TiO₂ layers of the BiPbTi₂O₆/PbTiO₃ heterostructure (the ordering is consistent with Fig. 5 in the main text). The orange dashed line is Fermi level, which is set to zero energy.

Supplementary Note 8. The charge leakage in BiPbTi₂O₆/ferroelectric heterostructure

We note that in Fig. 5 of our main text charge leakage into PbTiO₃ is non-negligible in the BiPbTi₂O₆/PbTiO₃ heterostructure. This charge leakage is due to “proximate effect” that PbTiO₃ has empty Ti d^0 states while BiPbTi₂O₆ has $0.5e$ in the d orbitals per Ti site. Charge transfer occurs from the Ti atoms in BiPbTi₂O₆ to the Ti atoms in PbTiO₃ thin films, a phenomenon similar to LaTiO₃/SrTiO₃ interface [13, 14]. To prevent charge leakage, we can use PbTi_{1-x}Zr_xO₃ (PZT) to replace PbTiO₃. The mechanism is that Zr has $4d$ orbitals, whose energy is higher than Ti $3d$ orbitals. To demonstrate that, we replace PbTiO₃ by PbZrO₃ in our heterostructure and re-do the calculations. Supplementary Figure 6 shows the conduction electrons in Ti- d and Zr- d orbitals. We find that charge leakage is completely suppressed and all the conduction electrons are confined in Ti- d orbitals in BiPbTi₂O₆. A direct simulation of PZT requires a much larger supercell and a proper treatment of random alloying, which is beyond the capability of our computation resources. However, the physics trend is clear: the more Ti atoms are replaced by Zr atoms, the weaker the charge leakage. Usually PZT with $x \sim 0.2 - 0.5$ is widely used in ferroelectric heterostructures [15–18].



Supplementary Figure 6. **DFT calculation of BiPbTi₂O₆/PbZrO₃ heterostructure.** **a** Atomic structure of the BiPbTi₂O₆/PbZrO₃ heterostructure: The red (green) arrow refers to PbZrO₃ polarization (BiPbTi₂O₆ polar displacements). **b** Layer-resolved conduction electrons on Ti and Zr atoms. The red dashed lines indicate the interface between PbZrO₃ and BiPbTi₂O₆.

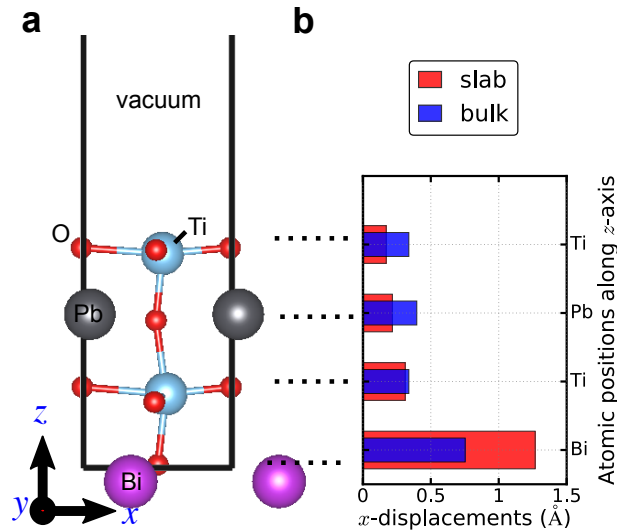
Supplementary Note 9. Polar displacements in thin films of polar metal $\text{BiPbTi}_2\text{O}_6$

There is “size effects” in ferroelectric thin films [19]. With the thickness of ferroelectric thin films decreasing, depolarization fields (if not fully screened) reduce and sometimes completely suppress the polarization [20, 21].

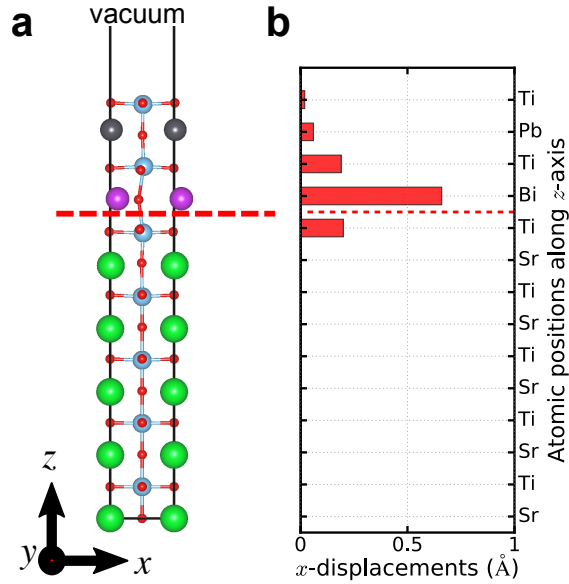
However, polar metals do not have such a “size effect” because free electrons in metals fully screen depolarization fields in both bulk and thin films. To support that, we perform two additional calculations.

The first calculation is a thought-experiment. We calculate a free-standing one unit cell $\text{BiPbTi}_2\text{O}_6$ thin film. We find that down to one unit cell, $\text{BiPbTi}_2\text{O}_6$ is still polar. The polar displacements of free-standing one unit cell $\text{BiPbTi}_2\text{O}_6$ thin film are shown in Supplementary Figure 7, which are compared to bulk $\text{BiPbTi}_2\text{O}_6$. This shows that there is no “size effect” in thin films of polar metal $\text{BiPbTi}_2\text{O}_6$.

The second calculation is to study “proximity effect” in $\text{BiPbTi}_2\text{O}_6$ thin films. Instead of a $\text{BiPbTi}_2\text{O}_6/\text{PbTiO}_3$ heterostructure, we calculate a $\text{BiPbTi}_2\text{O}_6/\text{SrTiO}_3$ heterostructure, in which SrTiO_3 is paraelectric. Supplementary Figure 8 shows the optimized structure in our DFT calculations and the corresponding polar displacements along x -axis. We find



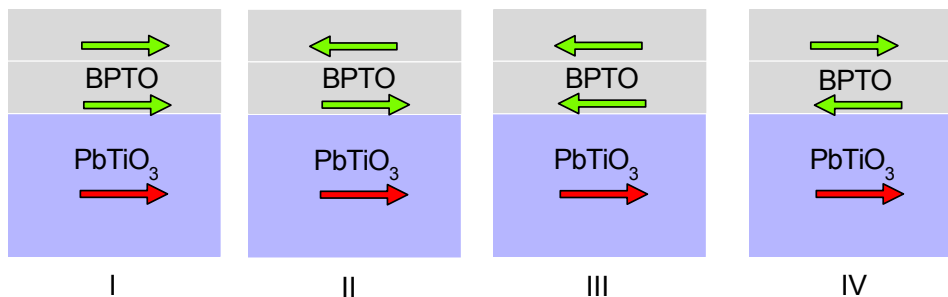
Supplementary Figure 7. **The structural property of free-standing one unit cell $\text{BiPbTi}_2\text{O}_6$ thin film.** **a** Optimized crystal structure. **b** The comparison of layer-resolved polar displacements between one unit cell $\text{BiPbTi}_2\text{O}_6$ thin film and the bulk phase.



Supplementary Figure 8. **The property of $\text{BiPbTi}_2\text{O}_6/\text{SrTiO}_3$ interface.** **a** The optimized structure of $\text{BiPbTi}_2\text{O}_6/\text{SrTiO}_3$ interface. The vacuum layer is about 15 Å in our DFT model. **b** The polar displacements along x -axis in $\text{BiPbTi}_2\text{O}_6/\text{SrTiO}_3$ interface. The dashed red lines indicate the interface between $\text{BiPbTi}_2\text{O}_6$ and SrTiO_3 .

that the polar displacements in $\text{BiPbTi}_2\text{O}_6$ still exist. In addition, the structural coupling between $\text{BiPbTi}_2\text{O}_6$ and SrTiO_3 drives the interfacial Ti atom in SrTiO_3 to be polar (see Supplementary Figure 8). This indicates that the polar displacements in $\text{BiPbTi}_2\text{O}_6$ thin films are *not* due to proximity coupling with PbTiO_3 . In fact, they are so strong that they can drive a paraelectric material (such as SrTiO_3) to be polar close to the interface.

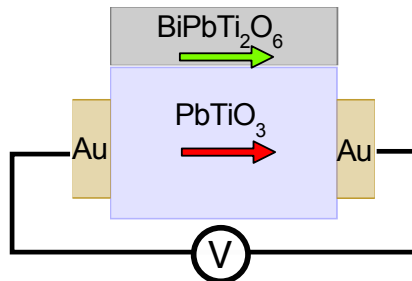
Supplementary Note 10. Switching of multi-layer BiPbTi₂O₆ films



Supplementary Figure 9. **Switching of multi-layer BiPbTi₂O₆ thin films.** Four different configuration of the heterostructure composed of PbTiO₃ thin film and two unit cells of BiPbTi₂O₆. The red arrow refers to the polarization of PbTiO₃ thin film. The green arrows refer to the polar displacements of *each* unit cell of BiPbTi₂O₆.

To support the physical picture of switching multi-layer BPTO in the main text, we perform calculations of two-unit-cell BPTO thin films on PbTiO₃. Supplementary Figure 9 shows different configurations of polar displacements of BPTO and polarization of PbTiO₃. The red arrow is the polarization of entire PbTiO₃ thin film. The green arrow refers to the polar displacements of *each* unit cell of BPTO. Since there are two unit cells of BPTO, then there are altogether four different configurations. Our calculations find that their total energies are $E_I < E_{II} < E_{III} < E_{IV}$. This energy order is easy to understand: both the interface and bulk BPTO prefers to have a parallel coupling between polar displacements and polarization. In configuration I, both the polar displacements of BPTO between the two unit cells and the polarization of PbTiO₃ are parallel, which leads to the lowest total energy. In configuration IV, the polar displacements of BPTO between the two unit cells are *antiparallel*. The polar displacements of the bottom layer BPTO is also *antiparallel* to the polarization of PbTiO₃. The two antiparallel couplings combined result in the highest total energy. The switching process is as follows: we start from configuration III in which the polarization of PbTiO₃ is switched by an electric field. The interfacial coupling drives the bottom unit cell of BPTO to switch its polar displacements (*i.e.*, configuration II). Then the bulk coupling in BPTO drives the top unit cell of BPTO to switch its polar displacements (*i.e.*, configuration I). This entire process is favored by thermodynamics because the total energy monotonically decreases from configuration III to II and finally to I.

Supplementary Note 11. Uniform strain in epitaxial $\text{BiPbTi}_2\text{O}_6$ thin film from experimental perspective



Supplementary Figure 10. **A model device based on $\text{BiPbTi}_2\text{O}_6/\text{PbTiO}_3$.** Au only works as electrode.

In our DFT calculations, the BPTO/ PbTiO_3 heterostructure is simulated by constraining its in-plane lattice constant to that of KTaO_3 substrate ($a = 4.00 \text{ \AA}$, see Supplementary Table II). The entire heterostructure is under *uniform* tensile strain. Under this strain, the $Pmm2$ perovskite phase is indeed stabilized (see Fig. 4 in the main text). We find the metastable (even unstable and unusual polymorphs) phase can appear via applying uniform epitaxial strains to thin films [22–25]. Such epitaxial stabilization can be understood by the theory of free energy minimization, in which the energy of coherent and semicoherent interfaces is much lower than that of noncoherent ones [26]. Therefore, the formation of low-energy interfaces and the minimization of overall free energy of the system due to the contribution of volume strain energy usually give rise to the experimentally observed metastable and even unstable structures.

Specifically for oxide heterostructures, experimentalists find that the critical thickness below which the entire thin film is under *uniform* strain is typically about 10 nm and sometimes can exceed 100 nm [27]. In our case, the thickness of BPTO/ PbTiO_3 heterostructure (in Fig. 4 in the main text) is only 4 nm, which is far below the critical thickness for uniform strain. Furthermore, in our BPTO/ PbTiO_3 heterostructure, PbTiO_3 has a polarization parallel to the interface. This means that the depolarization field in PbTiO_3 thin film can be fully screened by the two electrodes (see the “toy device” in Supplementary Figure 10). Therefore the thickness of PbTiO_3 films can be further reduced without suppressing its polarization. Based on the above reasons, our BPTO/ PbTiO_3 heterostructure is anticipated

to be uniformly strained and thus can be stabilized on KTaO_3 or NdScO_3 substrate.

-
- [1] King, G. & Woodward, P. M. Cation ordering in perovskites. *J. Mater. Chem.* **20**, 5785–5796 (2010).
- [2] Biswas, A., Yang, C.-H., Ramesh, R. & Jeong, Y. H. Atomically flat single terminated oxide substrate surfaces. *Prog. Surf. Sci.* **92**, 117–141 (2017).
- [3] Bansal, D., Aref, A., Dargush, G. & Delaire, O. Modeling non-harmonic behavior of materials from experimental inelastic neutron scattering and thermal expansion measurements. *J. Phys. Condens. Matter* **28**, 385201 (2016).
- [4] Grimvall, G. *Thermophysical Properties of Materials*, (Elsevier, Amsterdam, 1999).
- [5] Zhu, L.-F. et al. Ab initio based study of finite-temperature structural, elastic and thermodynamic properties of FeTi. *Intermetallics* **45**, 11–17 (2014).
- [6] Grabowski, B., Ismer, L., Hickel, T. & Neugebauer, J. Ab initio up to the melting point: Anharmonicity and vacancies in aluminum. *Phys. Rev. B* **79**, 134106 (2009).
- [7] Mermin, N. D. Thermal properties of the inhomogeneous electron gas. *Phys. Rev.* **137**, A1441–A1443 (1965).
- [8] Bruce, P. G. *Solid State Electrochemistry*, (Cambridge University Press, Cambridge, 1997).
- [9] Togo, A. & Tanaka, I. First principles phonon calculations in materials science. *Scr. Mater.* **108**, 1–5 (2015).
- [10] Mounet, N. & Marzari, N. First-principles determination of the structural, vibrational and thermodynamic properties of diamond, graphite, and derivatives. *Phys. Rev. B* **71**, 205214 (2005).
- [11] Zhong, W., King-Smith, R. D. & Vanderbilt, D. Giant LO-TO splittings in perovskite ferroelectrics. *Phys. Rev. Lett.* **72**, 3618–3621 (1994).
- [12] Dawber, M. et al. Unusual behavior of the ferroelectric polarization in $\text{PbTiO}_3/\text{SrTiO}_3$ superlattices. *Phys. Rev. Lett.* **95**, 177601 (2005).
- [13] Ohtomo, A., Muller, D. A., Grazul, J. L. & Hwang, H. Artificial charge-modulation in atomic-scale perovskite titanate superlattices. *Nature* **419**, 378 (2002).
- [14] S., O. & A.J., M. Electronic reconstruction at an interface between a mott insulator and a band insulator. *Nature* **428**, 630 (2004).
- [15] Zhang, Y. et al. Discovery of a magnetic conductive interface in $\text{PbZr}_{0.2}\text{Ti}_{0.8}\text{O}_3/\text{SrTiO}_3$

- heterostructures. *Nat. Commun.* **9**, 685 (2018).
- [16] Choi, J. et al. Different nonvolatile memory effects in epitaxial Pt/PbZr_{0.3}Ti_{0.7}O₃/LSCO heterostructures. *Appl. Phys. Lett.* **96**, 262113 (2010).
- [17] Feigl, L., Misirlioglu, I. B., Vrejoiu, I., Alexe, M. & Hesse, D. Impact of misfit relaxation and a-domain formation on the electrical properties of tetragonal PbZr_{0.4}Ti_{0.6}O₃/PbZr_{0.2}Ti_{0.8}O₃ thin film heterostructures: Experiment and theoretical approach. *J. Appl. Phys.* **105**, 061607 (2009).
- [18] Wang, G. S. et al. PbZr_{0.5}Ti_{0.5}O₃/La_{0.5}Sr_{0.5}CoO₃ heterostructures prepared by chemical solution routes on silicon with no fatigue polarization. *Appl. Phys. Lett.* **79**, 3476–3478 (2001).
- [19] Li, S. et al. Dimension and size effects in ferroelectrics. *Jpn. J. Appl. Phys.* **36**, 5169–5174 (1997).
- [20] Batra, I. P. & Silverman, B. Thermodynamic stability of thin ferroelectric films. *Solid State Commun.* **11**, 291–294 (1972).
- [21] Junquera, J. & Ghosez, P. Critical thickness for ferroelectricity in perovskite ultrathin films. *Nature* **422**, 506 (2003).
- [22] Trampert, A., Brandt, O., Yang, H. & Ploog, K. Direct observation of the initial nucleation and epitaxial growth of metastable cubic GaN on (001) GaAs. *Appl. Phys. Lett.* **70**, 583–585 (1997).
- [23] Xu, Y. et al. Strain-induced metastable phase stabilization in Ga₂O₃ thin films. *ACS Appl. Mater. Interfaces* **11**, 5536–5543 (2019).
- [24] Damodaran, A. R., Lee, S., Karthik, J., MacLaren, S. & Martin, L. W. Temperature and thickness evolution and epitaxial breakdown in highly strained BiFeO₃ thin films. *Phys. Rev. B* **85**, 024113 (2012).
- [25] Sando, D., Xu, B., Bellaiche, L. & Nagarajan, V. A multiferroic on the brink: Uncovering the nuances of strain-induced transitions in BiFeO₃. *Appl. Phys. Rev.* **3**, 011106 (2016).
- [26] Gorbenko, O. Y., Samoilenkov, S. V., Graboy, I. E. & Kaul, A. R. Epitaxial stabilization of oxides in thin films. *Chem. Mater.* **14**, 4026–4043 (2002).
- [27] Wang, T., Ganguly, K., Marshall, P., Xu, P. & Jalan, B. Critical thickness and strain relaxation in molecular beam epitaxy-grown SrTiO₃ films. *Appl. Phys. Lett.* **103**, 212904 (2013).